Aalto University
School of Science
Degree Programme in Applied Physics

Jared Myren

Wetting of Cryoliquid Droplets:
Non-Boiling & Leidenfrost States

Master's Thesis
Espoo, March 17, 2016

Supervisor: Professor Robin Ras

Aalto University
School of Science
Degree Programme in Applied Physics

ABSTRACT OF
MASTER'S THESIS

Author: Jared Myren

Title:
Wetting of Cryoliquid Droplets: Non-Boiling & Leidenfrost States

Date: March 17, 2016 **Pages:** viii + 55

Major: Physics of Advanced Materials **Code:**

Supervisor: Professor Robin Ras

This thesis presents the development of an experimental setup and testing methodology for investigating the behavior of non-boiling droplets of cryogenic liquids (cryoliquids) on cooled, super-repellent surfaces, along with preliminary measurement results from experiments performed with liquid oxygen droplets. This work was made possible and inspired by recent developments in the fabrication of doubly re-entrant nanostructured surfaces capable of repelling low surface tension fluids at room temperature, as the surface tension of cryoliquids is similarly low. No free-standing repelled droplets were achieved in this study, however two droplets were repelled while in contact with the deposition tip, indicating the potential for future testing with doubly re-entrant sample designs using this experimental approach.

Additional experiments were also performed with liquid oxygen droplets in Leidenfrost states on smooth, room temperature substrates, utilizing the paramagnetism of liquid oxygen to observe low friction harmonic oscillations of droplets in a parabolic magnetic field. Analysis of these experiments showed that a modified model, originally developed for oscillating ferrofluid droplets on superhydrophobic surfaces, could be fit to oscillatory Leidenfrost droplet motion. The results suggest the potential for further studies investigating the interactions between magnetic forces and low friction droplet dynamics with low surface tension fluids.

Keywords: droplet, cryoliquid, oxygen, super-repellent, Cassie-Baxter, non-boiling, paramagnetism, Leidenfrost, evaporation

Language: English

Acknowledgements

I wish to thank my supervisor, Professor Robin Ras, along with the members of the Soft Matter & Wetting group, for encouragement, support, and advice during this thesis project. I also thank Dr. Xiaotao Zhu for working with me during much of the project and for his advice and friendship. I thank the Nanotalo Machine Shop personnel for their significant and timely contributions to the experimental setup used in this project. Additionally, I would like to thank Dr. Ville Jokinen, Ville Rontu, and Professor Sami Franssila of the Microfabrication group for their involvement in the project and for fabricating the sample surfaces.

I also thank my wife Sarah for her unending patience, encouragement, and delicious food.

This work was performed in the Nanotalo chemistry laboratories and with the cooperation of Nanotalo Microscopy Center (NMC), as well as the Micronova cleanroom and thin film laboratories. This thesis was performed as part of a project funded by the Aalto Center for Quantum Engineering (CQE).

Otaniemi, Espoo, March 17, 2016

Jared Myren

Glossary

Terms	Definitions (Order of Appearance)
Sessile Droplet	A fluid droplet deposited onto a horizontal sample surface.
Apparent Contact Angle (ACA)	The measurable angle between the droplet edge and the substrate, as measured from the contact point.
Local Contact Angle (LCA)	The contact angle at the microscopic region of the fluid-surface contact point, may differ significantly from the apparent contact angle.
Super-Repellency	A property of a surface which indicates a high contact angle will be observed for a sessile droplet of a given fluid.
Advancing & Receding Contact Angles	Dynamic contact angles measured during droplet expansion/reduction or from either side of a moving droplet on a substrate.
Contact Angle Hysteresis (CAH)	The magnitude of the difference between the advancing and receding contact angles, describes the mobility of a given droplet on a substrate.
Cryoliquid	A low boiling point fluid, typically elemental. Relevant examples: liquid oxygen and nitrogen.
Paramagnetism	Paramagnetic materials (e.g., liquid oxygen) form induced, impermanent, internal magnetic fields that exert an attractive force between the object and the magnet.
Dewar	An insulated vessel used for storing cryoliquids with minimal evaporative losses, typically multi-walled with evacuated and/or insulated layers.
Surface Tension	A fluid property describing the magnitude of the tension that drives surface area/energy minimization, stemming from the strength of the molecular interactions in the fluid.
Pinning	The behavior of a fluid-surface contact line which resists lift-off from that surface due to molecular interactions with that surface.
Cassie/Wenzel State	Terms describing a droplet on a structured surface being repelled with a high contact angle on top of the structures (Cassie) or penetrating the structures and contacting the substrate with a lower contact angle.
Cassie Fraction	The proportion of a structured surface in solid-fluid contact with a sessile droplet in a Cassie state on that surface.
Wetting Transition	The transition of sessile droplet from a Cassie state to a Wenzel or complete wetting state or vice versa, the cause can be deliberate or accidental and a wide variety of inducing mechanisms have been observed.
Axisymmetric Drop Shape Analysis (ADSA)	An analysis tool used to fit the Young-Laplace model to a sessile droplet profile and minimize fitting error for accurate determination of the contact angle.
Bond/Eötvös Number	A dimensionless number describing the relative importance of surface tension forces in a droplet to other forces such as gravity.
Constant Contact Radius/Angle (CCR/CCA)	The general stages of droplet evaporation on a repellent surface, the CA decreases to receding angle in CCR mode first, then the three-phase contact line retracts with a constant CA.

Stick-Slip Motion	When a droplet is evaporating on a structured surface with non-negligible CAH in CCA mode, the contact line moves in discrete jumps from structure to structure, resulting in a vacillating receding contact angle.
Break-In Pressure	The pressure limit for a sessile droplet resting on surface structures at which the droplet will undergo a wetting transition to a Wenzel or completely wetting state.
Weber/Reynolds Numbers	Fluid dynamical values that relate a given fluid's surface tension/viscosity with its inertia, useful for analyzing droplet impacts on surfaces.
Leidenfrost State	Fluid in contact with a surface heated to the Leidenfrost temperature for that fluid-surface pair will float on a cushion of its own evaporative vapor flux, significantly reducing evaporative heat transfer as well as sliding friction.

Contents

List of Figures

1 Introduction

The wetting behavior of fluid droplets on surfaces is a long-standing and active field of academic research and industrial development towards wide-ranging applications. A subset of this field that has grown to prominence over the past several decades is the study of low energy surfaces which are not wetted by fluid, but instead repel droplets, which "bead", minimizing the fluid-surface contact area. Such droplets can exhibit high mobility and the surfaces can remain dry even while in contact with the fluid. Such surfaces can even exhibit self-cleaning properties, as mobile droplets remove debris as they roll off. The development of repellent surfaces has been inspired by similar, naturally occurring surfaces, which are found in plants (e.g., lotus and cabbage leaves, rose petals), insects (e.g., mosquito eyes, cicada wings, water strider legs/feet), and even animals (e.g., bird feathers, geckos) [1]. Capacity for fluid repellency is governed by the fraction of the surface actually in physical contact with the liquid, the geometry of the surface roughness, the physical and chemical properties of the fluid and surface material, and, finally, environmental factors such as temperature, pressure, and any external forces. In this work we assume no fluid-surface chemical interactions and focus on inert substrate materials with fluid repellent properties stemming solely from the geometry of surface nanostructures. Low-energy surfaces fabricated with micro- and nano-scale structures can enable static or even dynamic fluid droplets to exist in non-wetting states *even if the substrate material is intrinsically* (i.e., with a flat geometry) *wetted by that fluid*.

The majority of experimental research into super-repellent surfaces has involved room-temperature fluid droplets in ambient conditions (or inert atmospheres at room temperature). The first focus of this work instead considers the behavior of low-boiling point *cryoliquid* droplets deposited onto cryogenically cooled, super-repellent substrates in environmentally controlled conditions towards applications in cryogenic storage and handling. This is a novel subject seemingly absent in existing droplet research literature. The second focus of this thesis investigates the *Leidenfrost* phenomena using oscillating, highly mobile, paramagnetic liquid oxygen droplets on room-temperature surfaces in the presence of magnetic fields. The methodology modified for use in the latter experiments had been previously developed for similarly oscillating ferrofluid droplets on superhydrophobic surfaces and enables studies of low friction droplet dynamics.

2 Background & Motivation

2.1 Contact Angle Terminology

Non-wetting droplets may be characterized by a variety of experimental methods, the most common being optical goniometry of a *sessile droplet* (a droplet resting on horizontal surface). This technique involves imaging a static or dynamic droplet on a surface under high contrast lighting and utilizing various image analysis techniques to determine the angles between the droplet edges and the substrate, measured from the point of contact (see Figure 1). This angle is reported as the *apparent contact angle* (ACA) for the specific liquid/surface combination under the specified testing conditions. Apparent contact angles are referred to as such in contrast with the *local contact angle* (LCA), which is the true angle observable in the microscopic area of the fluid-surface contact line, and the two angles may differ drastically depending on the specific surface properties and geometry. The local contact angle is difficult to measure in practice for most surfaces and in this work we concern ourselves solely with apparent contact angles, referred to herein simply as θ.

Surfaces which display contact angles of $\theta < 90°$ for water droplets are referred to as hydrophilic, while contact angles of $\theta > 90°$ label a surface hydrophobic. The high and low extremes of these behaviors are labeled superhydrophobicity ($\theta > 150°$) and superhydrophilicity ($\theta < 5°$), respectively. Surfaces which are highly repellent to oils are termed superoleophobic, surfaces which exhibit both superhydrophobicity and superoleophobicity are termed superamphiphobic, whilst surfaces which can repel a wider variety of liquids have been labeled superomniphobic [2, 3] or superlyophobic [4]. As the latter two terms misleadingly imply repulsion of *all* fluids (repulsion of superfluid helium, for example, is currently unattainable), the surfaces of interest in this work will be referred to simply as *super-repellent*.

A related metric often reported in literature for the characterization of droplets on repellent surfaces is the *contact angle hysteresis* (CAH), which describes the magnitude of the difference between *advancing* (θ_{adv}) and *receding* (θ_{rec}) contact angles. The advancing contact angle is measured while the droplet is expanding (increasing in volume) across the substrate or from the droplet's leading edge during sliding motion, while the receding angle is measured during deflation or from the trailing edge of a sliding droplet (see Figure 2). The receding angle is often cited as a more meaningful characterization of a surface as it is dependent only on the pinning behavior of the fluid on the surface structures, whereas the advancing angle is dependent also on the size of the droplet and the speed of contact line across the structures

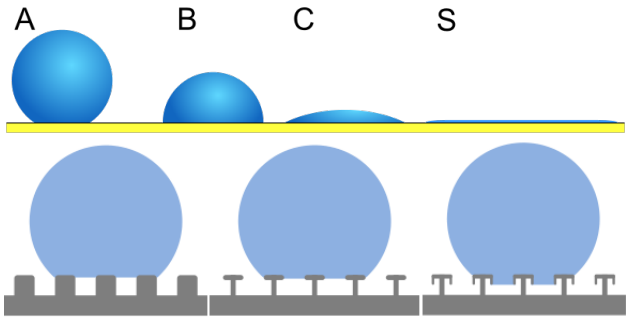

FIGURE 1: *Droplets exhibiting complete wetting (S) to hydrophilic (C) to mildly hydrophobic (B), to beading (A) on smooth surfaces (top). Bottom image shows super-repellent behavior possible on structured surfaces. Top image from Wikipedia, bottom adapted from [3].*

[5–7]. The CAH characterizes a droplet's mobility on a surface and indicates the strength of the microscopic pinning behavior. In fact, the CAH is often a more meaningful metric when characterizing a liquid-surface pair as it is less sensitive to deposition technique and less likely to be obscured by multiple stable (or even metastable) states in which equilibrium droplets may exist on a rough surface. Both the CA and CAH can be used to predict the behavior of a droplet (or even larger macro-quantities of liquid) on a particular surface, but in this work we will focus specifically on the effects of surface parameters on evaporation rates, which have been shown in many studies to be affected by the wetting properties of the liquid-surface pair.

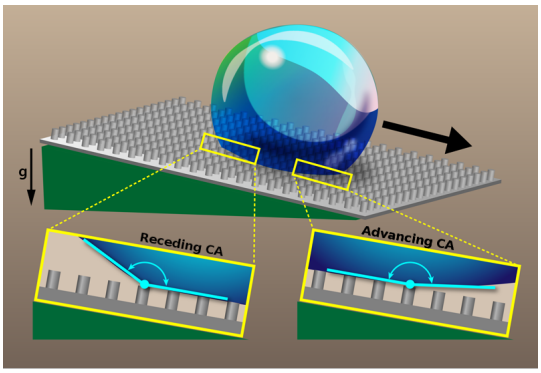

FIGURE 2: *The advancing contact angle is measured during droplet expansion or (as shown here) at the leading edge during sliding motion, the receding contact angle is measured during deflation or from the trailing edge during sliding motion. The CAH is defined as the difference between the two angles and characterizes the droplet's mobility on a given surface. Adapted from [1].*

2.2 Cryoliquids & Applications

Examples of cryoliquids include the widely utilized liquid nitrogen (LN_2), as well as other elemental fluids. This work particularly focuses on characterizing the behavior of liquid oxygen (LOX) droplets for several reasons: a) it is widely utilized in a variety of industrial and scientific applications, b) it can be easily produced in small amounts in laboratory settings, and c) it exhibits convenient boiling (90 K) and melting (5 K) points such that the liquid phase is stable in environments cooled to LN_2 temperatures (77–85 K). Interestingly, LOX also exhibits significant *paramagnetism*, allowing for magnetic droplet manipulation.

While some cryoliquids can be generated at the point of use, most scientific and industrial applications involve the operator simply drawing a needed amount from a storage reservoir which contains a larger quantity of cryoliquid maintained below its boiling point. The reservoir is typically insulated in large containers known as *dewars*, which typically have a layer of vacuum between their reflective walls (see Figure 3). Nevertheless, the stored liquid evaporates away over time due to radiative heat transfer through the vacuum layers and extraction points. A typical method of mitigating this effect is constructing multiply-layered walls within the dewar and/or using specially designed insulation materials and reflective coatings to lengthen the radiative and conductive pathways for evaporative heat to reach the cryoliquid. The rate of volume loss for a specific dewar is dependent on the volume and specific properties (latent heat of vaporization, boiling point) of the stored liquid and on the design of the storage dewar, but nonetheless can be significant, ranging from less than 1% up to 3% total mass loss per day [8].

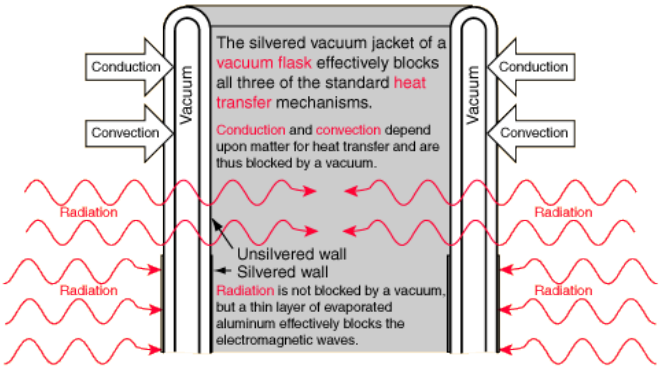

FIGURE 3: *A dewar's insulation capacity is determined by the design of its walls. The use of reflective surfaces and multiple walls with insulating layers of vacuum drastically decrease the evaporation loss from heat transfer. Image from [9].*

The *surface tension* of cryoliquids is uniformly low (to varying degrees) compared to that of water ($\approx 72\,\mathrm{mN/m}$). LOX's surface tension is 13–16 mN/m at 90–78 K [10, 11], which is comparable with the lowest known values attributed to room temperature fluids (fluorinated solvents) [3]. Low surface tension fluids typically exhibit very low contact angles on all substrates and thus, within a dewar, a cryoliquid will fully wet the inner surfaces, thereby maximizing the heat conduction rate. A super-repellent surface able to coat the inside of a dewar and maintain the cryoliquid in a non-wetting state could potentially reduce the amount of heat conducted directly to the fluid, adding another layer of insulation against evaporative losses. The controlled transportation of cryoliquids, including liquid oxygen, in spacecraft engines (where LOX is often used as a fuel oxidizer) could also benefit from reduced wetting in surface interactions within tanks and plumbing.

2.3 Super-Repellent Surfaces

Super-repellent surfaces reported in literature are typically unable to repel very low surface tension fluids ($\gamma < 20\,\mathrm{mN/m}$), however a recent development described by Liu and Kim [3] resulted in successful structural super-repellency of a perfluorohexane (FC-72) with a surface tension of 10 mN/m. This super-repellent behavior resulted from the *doubly re-entrant* topology of the surface structures (see Figure 4) whose vertical overhangs (also referred to as "serifs") presented effective *pinning* points for the droplets' contact lines in 2D (in 3D, the contact points can travel along the profile's rim and thus the surfaces exhibit low roll-off angles and low CAH). Specifically, the vertical serif features on the caps provide the ideal configuration for the surface tension of the fluid to counteract the wetting pressures (ambient, gravitation, and Laplacian), as explained in the next section.

Research into these doubly re-entrant geometries performed by Prof. Sami Franssila's Microfabrication group at Aalto University has adapted the fabrication process and yielded similarly structured surfaces. The doubly re-entrant surfaces utilized in this work were fabricated by Dr. Franssila's team in the Micronova cleanroom by the procedures explained in the Methods section (4) and supplemental information (A). Examples of the structures utilized in this work (and the evolution of their design) are shown in Figure 5.

There are no cases found in the literature involving non-boiling cryogenic droplets on repellent surfaces. Thus, the long-term goal of this novel project is to image and analyze free-standing liquid oxygen droplets in non-boiling states on super-repellent surfaces. To that end, this thesis describe the design and fabrication of an experimental setup and the development of mea-

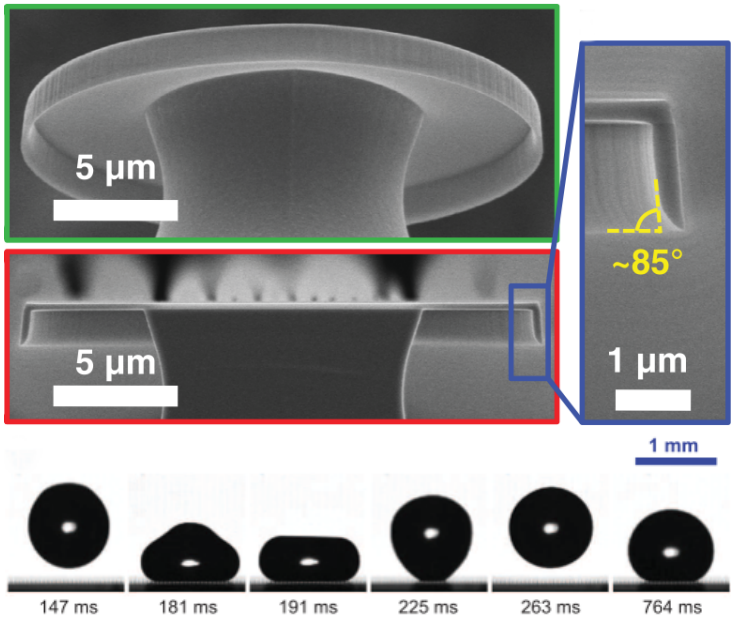

FIGURE 4: *Arrays of doubly re-entrant structures produced by Liu and Kim were shown to repel low surface tension fluids. Top image shows structure geometry and cross sections, bottom image shows an FC-72 droplet ($\gamma \approx 10\,\mathrm{mN/m}$) bouncing on a sample. Images adapted from [3].*

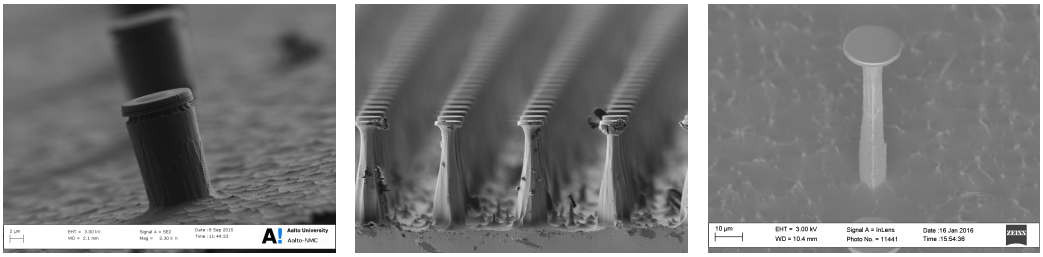

FIGURE 5: *Left to right: Initial samples with 10 µm cap diameters, scalloped sidewall texture stems from the Bosch etching process. 20 µm cap samples with fluoropolymer coating. Latest samples with improved geometry.*

surement methodologies for studying contact angles and evaporation rates for LOX droplets on doubly re-entrant substrates with varying surface parameters cooled to LN_2 temperatures in inert atmospheres under controlled environmental conditions. Preliminary testing results from several sample sets are described, though no free-standing droplets were achieved during this brief study. Additionally, preliminary analyses from experiments with highly mobile, non-contacting LOX droplets oscillating on room temperature substrates in the presence of a magnetic field are presented, utilizing

the methods developed by Timonen et al. [12].

3 Literature Review & Theory

3.1 Contact Angle Theory and Measurements

The prediction and experimental determination of contact angles for a given surface-droplet pair are entwined areas of active research with a history of scientific inquiry stretching back to the 19th century. In this section, a brief selection of literature and some common methods and models for measuring and/or predicting contact angles are presented. However, there are many more modeling and measurement techniques reported in literature, both established and recently developed, which are beyond the scope of this work and not mentioned here.

In the simplest configuration, a homogeneous smooth surface with a small droplet of pure fluid resting at equilibrium, the contact angle θ for a droplet is often described by a horizontal force balance (see Figure 6) given by the Young equation:

$$\gamma_{\mathrm{sv}} = \gamma_{\mathrm{sl}} + \gamma_{\mathrm{lv}} \cos\theta, \tag{1}$$

where γ_{ij} is the individual interfacial tension (typically in mN/m) between each of the solid, vapor, and liquid phases. The liquid-vapor interfacial tension is typically referred to simply as the surface tension γ of the fluid (assuming the vapor phase is (or is similar to) air).

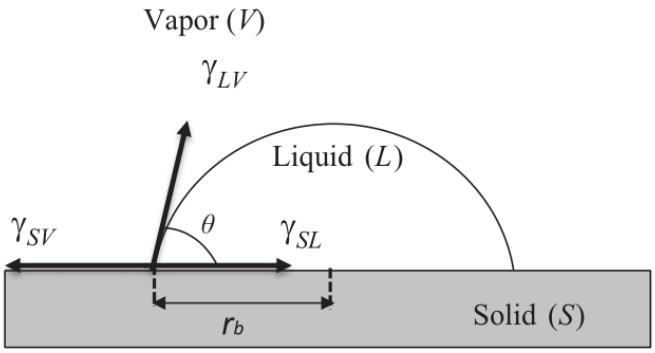

FIGURE 6: *For an ideal droplet on a perfectly smooth substrate, three forces acting on the three-phase contact line determine the contact angle: the vapor-liquid, the solid-liquid, and solid-vapor interfacial tensions. Image from [13].*

Rough homogeneous surfaces have apparent contact angles θ^* dependent on the surface roughness r (ratio of area in contact with droplet and projected

2D surface area under the droplet). If full contact with the droplet is assumed (i.e., no air pockets), the Wenzel equation:

$$cos\theta^* = r\cos\theta$$

can predict this apparent angle given knowledge of the smooth-geometry contact angle for the surface material. When the droplet does not fully wet a rough homogeneous surface, a version of the Cassie equation can be utilized [14]:

$$\cos\theta^* = r_{\text{loc}} f\cos\theta + f - 1,$$

where f is still the wetted surface fraction and r_{loc} is the surface roughness of only the wetted areas. These values, however, are often difficult to determine in practice.

For heterogeneous surfaces with defined areas of differing surface energies (due to chemical or structural differences), the Cassie-Baxter equation is often used to calculate contact angles:

$$\cos\theta^* = f_1\cos\theta_1 + f_2\cos\theta_2,$$

where f_{i} and θ_{i} are the area fraction and smooth geometry contact angle for each surface region in contact with the droplet (this equation is valid for a binary system as written but is easily expanded by summation to larger order systems). For a structured repellent surface, the second area is assumed to be the air between the structures with a 180° contact angle, so the C-B equation simplifies to its original formulation:

$$\cos\theta^* = f_1\cos\theta_1 - f_2. \tag{2}$$

According to Milne and Amirfazli [14], this is a more versatile and accurate formulation of the model for generalized structured surfaces, and it should be noted that, typically, $f_1 + f_2 > 1$ due to the deflection of the liquid surface (especially relevant to low surface tension fluids such as cryoliquids) in contact with the air between the structures. The f_1 value is often referred to as the *Cassie fraction* of a surface. It should also be noted that this deflection is not solely caused by any external normal forces (gravitation, magnetic fields, etc.) on the droplet, but also to the Laplace pressure within the droplet, described by the Young-Laplace equation:

$$\Delta P = \gamma\left(\frac{1}{R_1} + \frac{1}{R_2}\right), \tag{3}$$

where R_1 and R_2 are the principal radii of curvature for the droplet (simply the radius in the case of a spherical droplet). This pressure is, in fact,

typically dominant for small droplets (see the Wetting Transitions subsection below for more details).

The ubiquitousness of the Cassie-Baxter model has given rise to common terms of *Cassie* and *Wenzel states* in literature (see Figure 7, describing droplets repelled with a high contact angle on top of surface structures and droplets that have fully penetrated the structures and are in contact with the substrate, respectively. It should be noted that intermediate transition states have also been observed, in which droplets either become partially impaled on surface structures but do not (immediately) contact the substrate [15, 16] or wet into a portion of the contacted structures [17](these intermediate states are typically transient or metastable). The dynamics of wetting transitions is an active research field.

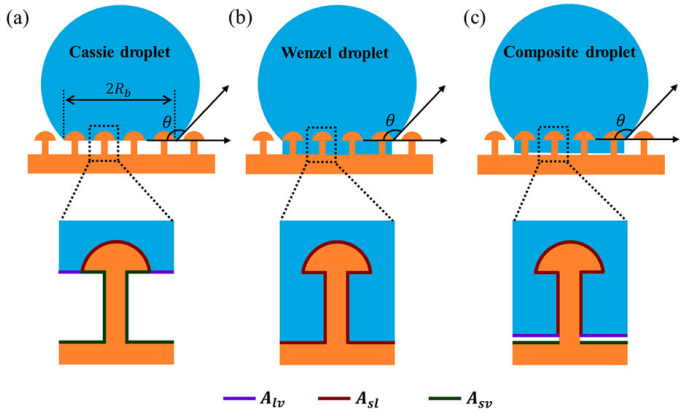

FIGURE 7: *A droplet (a) suspended on top of surface structures is said to be in a Cassie state, (b) a droplet with a measurable contact angle that has fully penetrated the structures is said to be in a Wenzel state, (c) an unstable/metastable droplet partially impaled onto the structures. Image from [17].*

A large debate in the past decade has focused on the overall validity of the Cassie-Baxter equations, with no general consensus having been reached as of yet. The crux of the argument stems from experiments performed by researchers such as Extrand, Gao, and McCarthy [13, 18], in which droplets were placed onto surfaces such that their three-phase contact lines rested on regions of differing surface energy than the regions in contact with the rest of droplet. These experiments showed that the three-phase contact line, rather than the entire contact area, determines the overall wetting behavior (namely, the contact angle) of the droplet, leading other researchers to formulate alternative versions of the Cassie-Baxter equations which replace the concept of area fraction with a calculated approximation of the contact line fraction [5]. However, this line fraction is difficult to measure accurately

in practice for surfaces not specially designed for such experiments, making model validation difficult. Additionally, arguments put forth *for* the validity of the Cassie-Baxter model suggest that the equations are only valid under certain assumptions, namely that the droplet size (or, more specifically, contact area) is large compared to the "wavelength", or characteristic length, of the surface structures (or any other heterogeneities) [19, 20]. A thorough review on this debate provides more detail [13].

3.1.1 Fitting/Prediction Models

It has been long reported that droplets under a certain size can be approximated with a spherical shape for the purposes of volume determination and contact angle modeling; this size is determined by the capillary length $\lambda_c = \sqrt{\gamma/\rho g}$, ($\approx 2.7\,\text{mm}$ for water at room temperature, $\approx 1.1\,\text{mm}$ for LOX at $90\,\text{K}$) where ρ is the fluid density. However, recent studies have shown that, especially for low surface tension fluids, this limit is inaccurate and droplets should be much smaller (pL scale) in order to avoid deformation by gravity [21, 22]. It should be noted that this approach would invite other, potentially more significant sources of error stemming from droplet evaporation and deposition feasibility/reliability, as well as necessitating extremely powerful optics for high resolution imaging of such small droplets, all of which may introduce similar (or larger) magnitudes of error compared to the small deformations resulting from gravitational forces.

The Young-Laplace model is commonly used to either predict the contact angle for a given fluid droplet on a surface or used to fit the droplet profile from an experimental image and extract the droplet parameters (size, curvature, etc.) needed to determine the contact angle. The Young-Laplace model is derived from the Laplace pressure equation (3), the pressure is equated to the hydrostatic pressure difference within and outside the droplet $\Delta P = \Delta\rho g z$, where z is direction normal to the substrate (this assumes an axisymmetric droplet shape) and $\Delta\rho$ is difference in density between the liquid and vapor phases. The curvature values R_1 and R_2 are rewritten in terms of 2D Cartesian coordinates, resulting in a differential equation (or an array of nonlinear partial differential equations), which can be written as [23, 24]:

$$(\Delta\rho)gh = \gamma\left[\frac{z''}{(1+z'^2)^{3/2}} + \frac{z'}{(1+z'^2)^{1/2}}\right], \tag{4}$$

where h is the z-coordinate at the droplet apex. Solutions to the Young-Laplace equation are numerical approximations, as no closed form solution exists. The first such numerical solution came from Bashforth and Adams [21,

24], who rewrote the Young-Laplace equation in dimensionless form (scaled with the capillary length) in an x-z coordinate system with the origin at the droplet apex with $Z = z - h$, b being the radius of curvature at the apex, and ϕ being the angle seen in Figure 8:

$$\frac{1}{R_1/b} + \frac{\sin\phi}{x/b} = 2 + \frac{\beta Z}{b}, \tag{5}$$

where, $\beta = \rho g b^2 \gamma^{-1}$ is known as the *Bond* (or *Eötvös*) number. In 1883, Bashforth and Adams computed numerical solutions (by hand) of values of x/b and z/b for large ranges of values of ϕ and β [25].

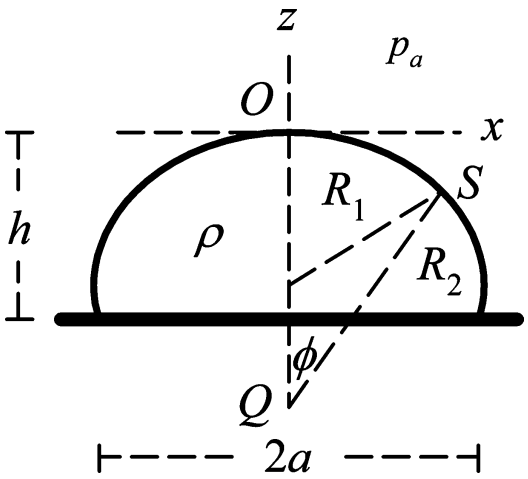

FIGURE 8: *The coordinate system utilized by Bashforth and Adams in their formulation of solutions to the Young-Laplace equation. Image from [21].*

In practice, different methods and models can produce calculated or predicted contact angles contradicting one another, as they often rely on human intervention to locate droplet contact points, baselines, or curvatures from experimental images. Other methods of predicting contact angles have been developed, though none have completely eliminated errors from human perception or proven useful for a wide range of fluids and surface types. One study has even derived an algorithm for choosing the most appropriate contact angle determination method for any given experiment [26].

A common modern method for fitting droplet profiles with the Young-Laplace model is the *axisymmetric drop shape analysis*, or ADSA, technique. In this technique, the experimental droplet profile is detected by the user or with software and compared to the ideal Young-Laplacian fit of the droplet. The sum of the squares of the differences between the experimental profile and model-generated droplet profile is then minimized by a nonlinear regression

procedure, yielding an optimal fit of the model profile to the experimental data and, finally, an accurate calculation of the contact angle. This method is not drop size dependent and does not require information about the droplet's apex, which can be difficult to determine for low surface tension fluids and/or large droplets. Many variants of the ADSA technique have been developed for different experimental configurations [27, 28].

A method developed by Srinivasan et al. [29] at MIT is based on a perturbation solution to the Bashforth-Adams model in which the nondimensionalized B-A equation is rewritten as two differential equations for the horizontal and vertical droplet edge coordinates. This technique requires only the maximum height and width of the droplet and produces comparably accurate contact angle determinations to the original exact Bashforth-Adams formulations, provided the Bond number is low enough, that is, that the droplets are not too large, nor is the surface tension too low. While the inputs still require image analysis techniques, the height and width are significantly easier to determine than the exact contact points for droplets with high contact angles for reasons explained in the next section.

Yet another technique, developed by Santini et al. [30], utilized a 3D measurement method based on x-ray tomographic imaging of droplets. In this method, a rotating sample stage was placed in a typical measurement configuration, but imaged with an x-ray source and detector instead of visible light and a standard camera. A 3D model (see Figure 9) was then reconstructed from 2D slices of scanning data and contact angle determinations were made from cross-sectional images.

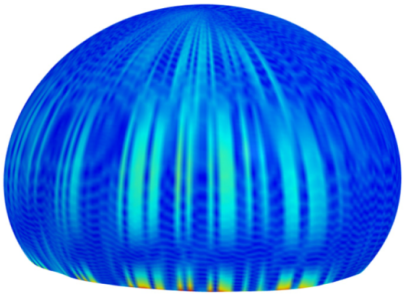

FIGURE 9: *X-ray tomography can yield an accurate 3D model of a sessile water droplet, allowing for cross-sectional contact angle averaging for decreasing measurement uncertainty. The color scale indicates error (max: 3.85%) in the Young-Laplace model fit to the experimental droplet profiles. Image adapted from [30].*

The cross sectional droplet profiles were fitted with the ADSA method [30], utilizing the Young-Laplace equation written in arc-length coordinates. This 3D technique allows many contact angle data points to be collected

for each individual droplet and averaged to produce more reliable measurements, while at the same time providing a measure of the axisymmetry of the three-phase contact line, potentially useful for mapping wetting behavior on regularly structured surfaces. Because any 2D analysis technique can be used for the contact angle determination, this method could act as a complement to many of the other approaches mentioned here.

3.1.2 Measurement Techniques & Limitations

Sessile droplets are typically analyzed by capturing images of them from the side under high contrast backlighting. The first studies [31] of contact angles involved platinum wires, lamps, and hand-held protractors; the experimental results relied solely on the judgment of the operator for accurate measurements. Current measurement techniques that utilize free-standing sessile droplets are conceptually quite similar to those early experiments, although the accuracy and precision of the instrumentation has improved greatly. Resulting images and videos can be analyzed during the experiment and/or afterwards by image analysis techniques and fit with theoretical models such as the Young-Laplace, Bashforth-Adams, or other models. This technique has proven to be acceptably accurate and repeatable (typical uncertainty of 2°) for droplets exhibiting contact angles below 160°. However, these methods often still rely on some user input and imperfect image analysis techniques for edge detection and location of the droplet contact points and/or baseline for determination of contact angle.

It has been shown that for super-repellent surfaces supporting contact angles above 160°, that while a 2° accuracy level is possible within an individual method, comparisons *between* various methods yielded significant disagreements [29, 32, 33], with the incongruities worsening with higher contact angles. For very large contact angles($\theta^* > 170°$), it becomes exceedingly difficult to accurately measure contact angles from images of sessile droplets. Many sources of error must be accounted for in these measurements: image resolution limits, diffraction-based optical defects in images (the space near the contact point can be so thin so as to cause the light passing through to be diffracted), and, importantly, the effect of local contact line deformations [5]. Another common source of measurement error for droplets with high contact angles ($\theta^* > 160°$) is that of substrate occlusion of the contact points caused by minute levels of tilt of the sample stage [33]. It is extremely difficult to perfectly align the camera, sample stage, and light source in order to image a droplet from the side and in practice most images are taken with the substrate tilted towards the camera at a small relative angle to avoid blurring of the contact line by the out-of-focus foreground of the surface structures.

An example of a typical image of a sessile droplet is shown in Figure 10. In the case of a stage tilted towards the camera, the image lighting needs to provide high enough contrast between the out-of-focus substrate *behind* the droplet base and the contact points in order to facilitate accurate location of the droplet baseline.

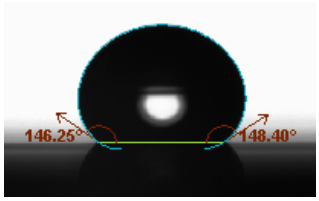

FIGURE 10: *A typical high contrast image of a sessile droplet (ethanol here on a doubly re-entrant surface) allows for edge detection, model fitting (here by the Young-Laplace model), and contact angle determination.*

These potential error sources highlight the inherent limits of techniques reliant on image analysis and the importance of camera resolution for high contact angle measurements with sessile droplets. When a typical image is generated, each pixel contains a value, the scale of which depends on the image type; the simplest, a gray-scale 8-bit image, contains pixels with values ranging from 0 to 255. An edge in the image will not, however, be shown as drastic single-pixel value change, a gradient will be present, especially if the background is not the light source directly (as is the case when the contact point is back-shadowed by the tilted substrate) and a threshold value supplied manually or calculated automatically by a wide variety of algorithms in analysis software will arbitrarily determine the location of the droplet edge.

The problem of localized contact angle variation is important especially for structured surfaces with large surface wavelengths, as the contact angle at the microscopic level near the contact points depends on the position of the camera, that is, whether the focal plane of the camera highlights a structure or a gap between the structures at the contact points. In the samples utilized in this thesis, the structures are comprised of silicon oxide (SiO_2), a naturally hydrophilic material. Liu and Kim showed [5] that the local contact angle on a hydrophilic surface can differ significantly from the apparent contact angle of the droplet on a structured surface comprised of the same material, making determination of the appropriate contact point in an image obviously difficult. This phenomenon may also play a role in *wetting transitions* and the dynamics of the receding contact angle, as illustrated in [5] and Figure 11.

Many sources of error mentioned here result from difficulties in accurately locating edges, contact points, and/or droplet baselines, and, for large con-

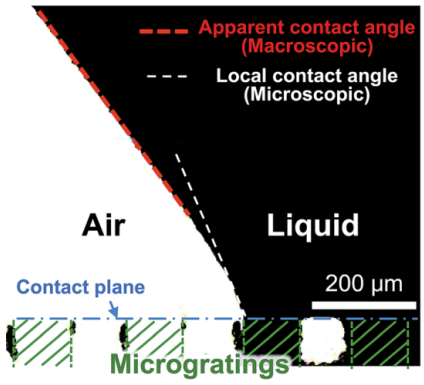

FIGURE 11: *For structured repellent surfaces composed of high surface energy materials, the apparent and local contact angles can vary significantly, making accurate comparisons of data difficult. Image adapted from [5].*

tact angles, a small error in contact line/point determination can lead to a significant mis-measurement of a droplet's apparent contact angle. The potential magnitude of the uncertainty resulting from inherent limitations of image analysis techniques is illustrated for a water droplet resting on a superamphiphobic surface in Figure 12. It is obvious that comparisons of high contact angle measurement data between experiments utilizing differing cameras, light sources, and/or software can be unreliable, even when testing similar fluids and surfaces.

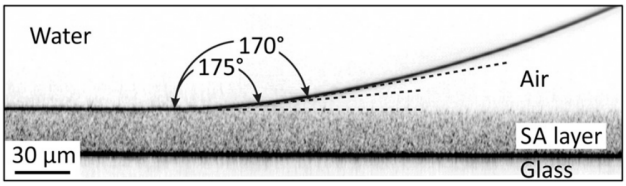

FIGURE 12: *For droplets with $\theta > 170°$, small errors in contact point location can result in significant uncertainty in θ determination. Image from [32].*

Further complications arise from the small droplet sizes used in most experiments because, while many contact angle fitting and prediction models assume small droplet sizes (sub-millimetric in diameter), validating these models requires powerful optics to reliably image such small droplets at high resolutions. In this work, contact angles are declared only as approximations due to the impracticality to account for all significant sources of error with our setup.

3.2 Evaporation Theory

The evaporation of sessile droplets from various surface types is the subject of a large body of literature reaching back over a century [34]. Recent work has focused on repellent and super-repellent surfaces, especially on nanostructured surfaces [35]. Not only does studying evaporating sessile droplets shed light on the substrate's thermal properties, it also provides an alternative method of determining the dynamic receding contact angle without disturbing a droplet's surface with a needle or requiring the substrate to be tilted accurately (to determine the start of rolling movement and thus the roll-off angle).

The evaporation process is not easily modeled for Cassie state droplets and is highly dependent on environmental factors such as ambient temperature, pressure, and the properties of the fluid and atmosphere. The flux of evaporating fluid is non-uniform across the droplet's surface area (except for droplets with vertical contact angles ($\theta = 90°$)) due to the temperature gradients resulting from thermal interactions with the substrate and the constraints of droplet-surface geometry for high contact angles [36, 37], as illustrated in Figure 13. The flux near the droplet-surface contact line is predicted to be larger than the average flux for droplets with low contact angles, while it is smaller than average for droplets exhibiting high contact angles. Direct experimental measurement of the local flux profile is difficult as it requires accurate determination of the liquid vapor concentration gradient locally at the droplet edge. The dynamics of this flux and the resulting pressure gradients can lead to interesting phenomena [38].

For any repellent surface (smooth or structured) with a measurable contact angle hysteresis for a given fluid, droplet evaporation occurs in two distinct stages: *constant contact radius* (CCR) and *constant contact angle* (CCA). The CCR stage begins as soon as the droplet is deposited. The three-phase contact line is effectively pinned to the surface and the contact angle decreases linearly as the droplet evaporates. For an ideal droplet on a flat surface, when the contact angle equals the receding angle, it holds constant and the CCA stage begins. The contact line then recedes axisymmetrically, diminishing the droplet's contact area. Due to the reduced heat transfer through the decreased contact area, the droplet begins evaporating more slowly during this stage. Several studies [35–37, 39] have presented models for predicting contact angles, volumes, and contact radii/area during both stages based on vapor-diffusion models derived from the Young-Laplace equation in toroidal coordinates.

On periodically structured surfaces, the CCA stage is characterized by *stick-slip* motion, in which the receding contact line "sticks" (pins) on each

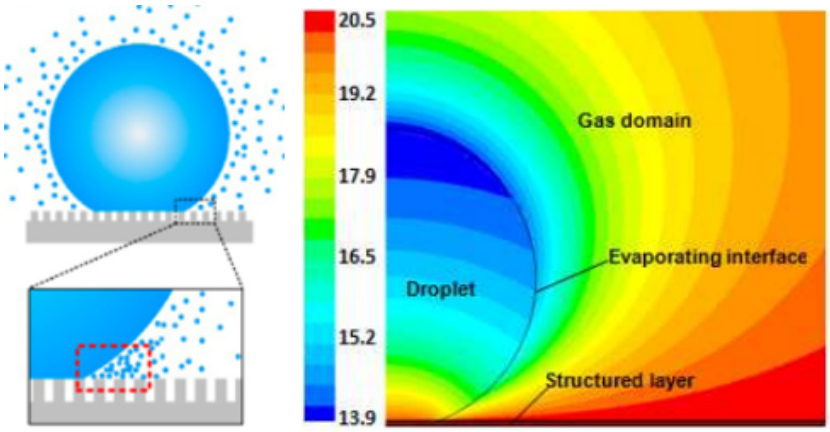

FIGURE 13: *The evaporative vapor surface flux from a droplet is nonuniform. The flux gradient is dependent on heat transfer from the substrate and is predicted to be lowest at the contact line. The size of the droplet and its contact angle controls the magnitude of this gradient. Left image from [39], right from [36].*

structure for a short time before "slipping" in a quick jump to the next structure. Stick-slip motion is easily identified from experimental data, as the apparent contact angle does not stay constant but rather vacillates sharply, as illustrated in Figure 14. This behavior was observed with water droplets deposited onto the doubly re-entrant surface structures in this work as well.

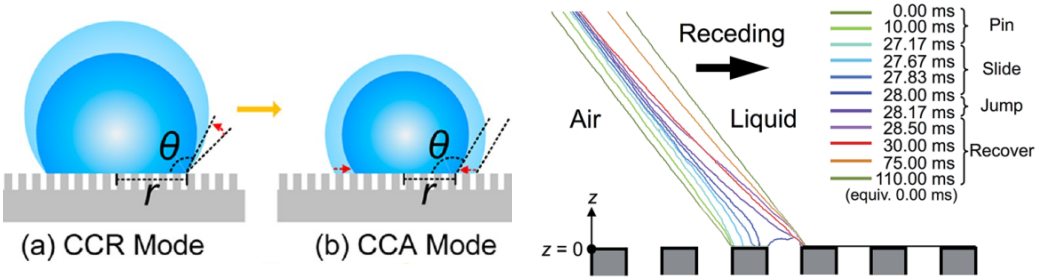

FIGURE 14: *Left: A droplet may evaporate in one of two stages (or both in series), constant contact radius (CCR) or angle (CCA). Right: A receding contact line moving across a surface with large enough structures (significant compared to the droplet's characteristic length) will move in a discrete fashion as the line adheres to a structure, is pulled across it, and jumps to the next structure. Left image from [39], right from [5].*

Droplets on super-repellent surfaces have been shown to evaporate more slowly than theoretical predictions which hold for normal repellent substrates [37], likely due to evaporative cooling of the droplet locally at the contact line. The impact of this effect on experimental data is determined by the properties

of the surface and fluid and can be mitigated by applying a simple correction factor to prediction equations [36]. The evaporation rates of droplets on repellent and super-repellent surfaces are not linear and droplet volume over time has been shown [36] to generally follow a relative power law:

$$V^{*2/3} = 1 - t^*, \tag{6}$$

where $V^* = V/V_{\text{initial}}$, $t^* = t/t_{\text{tot}}$, and t_{tot} is the total evaporation time. If the absolute volume data is linearized by this power law, the resulting slope has been found to depend on the Cassie fraction of the surface [39], that is to say, surfaces with lower Cassie fractions exhibit slower heat transfer rates and thus longer droplet lifetimes. This trend was also observed with water droplets on the doubly re-entrant surfaces studied in this work.

3.3 Wetting Transitions

A sessile droplet at equilibrium supported in a Cassie state on a structured surface can undergo a wetting transition to a Wenzel state or even completely wet the surface ($\theta^* \approx 0°$) by a variety of mechanisms. Dynamic transitions can occur with sliding droplets, as they encounter a defect or the three-phase contact lines become highly deformed.

Droplets in ambient conditions exert pressure on a surface due to the Laplace pressure, calculated from the Young-Laplace equation (4) (or approximated for very small droplets by $\Delta p = 2\gamma R^{-1}$, where R is the radius of curvature at the droplet's apex), which increases as the droplet evaporates. Large droplets also exert non-negligible pressures from the gravitational force. The pressure required to initiate a wetting transition on a structured surface is known as the *break-in pressure* and, according to Liu and Kim [3], can be calculated for a square unit of four doubly re-entrant structures with serif thickness t (see Figure 15) by

$$\Delta p_{\max} = \frac{\gamma \pi D'}{P^2 - \pi D'^2/4} \sin\alpha, \tag{7}$$

where $D' = D - 2t$ is the diameter of the contact line at the bottom of the cap's serif, P is the structure pitch, and α is the angle of the serif from the horizontal ($\alpha = \pi/2$ for perfectly vertical serifs). The critical pressure for a generalized fluid droplet on a generalized surface has been studied, but expressions found in the literature [1, 4, 15, 16, 32]) differ from one another (and even contradict in some cases). An inherent difficulty in experimentally determining this pressure is the sensitivity of such tests to surface defects and impurities, as wetting transitions do not need to be triggered by surface

conditions under the entire contact area; a single, localized defect can trigger a localized wetting transition which then causes a cascading wetting reaction for the entire droplet.

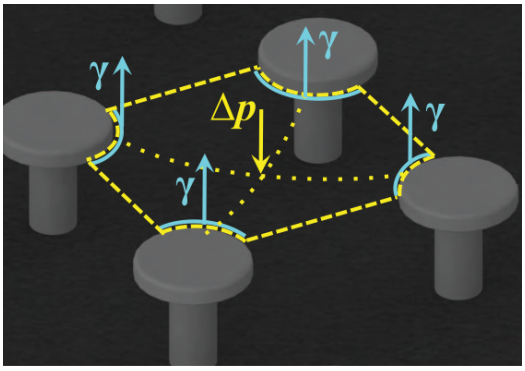

FIGURE 15: *The pressure acting on one unit cell of four structures can be used to calculate the pressure limit for a single structure. Image from [3].*

This Laplace pressure can cause a wetting transition either by forcing impalement of the droplet onto the surfaces or by deflecting the inter-structure droplet surface far enough to contact the substrate [16]. In the former case, additional pressure (though lower than the initial transition pressure) is required for the droplet to reach the substrate and fully wet the surface, this depends on the wetting properties of the structure sidewalls. The latter case is only common for structures with large pitch and small height, as the vertical deflection is relatively small for most fluids.

Some studies [2, 17] have shown that, for higher surface tension fluids, super-repellent surfaces can prevent a wetting transition from occurring even when the droplet evaporates entirely. Liu and Kim [3] showed that wetting transitions occurred approximately at the expected droplet size and Laplace pressure (60–65 Pa for 100 µm array pitch) for perfluorohexane (FC-72) droplets on doubly re-entrant structured surfaces. However, droplets impacting on surfaces will exert higher local pressures than static droplets and, therefore, falling droplets which are either too large to exert high Laplace pressures or too small to exert large pressures from gravitational forces at rest can undergo wetting transitions on structured surfaces upon impact. Such dynamic droplets are often characterized by their *Weber (We)* and/or *Reynolds (Re)* numbers to predict fluid dynamical effects and droplet deformations during impacts. The Weber number

$$We = \rho D v^2 / \gamma,$$

where D is the droplet diameter and v is the impact velocity, relates a

droplet's surface and kinetic energies, whereas the Reynolds number

$$Re = \rho D v / \eta$$

relates the impact velocity to the droplet's viscosity.

A phenomenon observed during preliminary manual testing with droplets of various solvents (dodecane, hexane, etc.) in this study was a "timed" wetting transition. A droplet would be deposited in a Cassie state and come to rest for a consistent duration (specific to that fluid and on the scale of seconds) before suddenly transitioning to a Wenzel state. The mechanism behind this phenomenon is unknown and the issue seems unaddressed in literature. A hypothesis which could be tested in future work is that the liquid is slowly wetting around the structures' surfaces and down to the substrate by means of a thin film spreading slightly faster than it evaporates. Another hypothesis is that the evaporated fluid vapor from the underside of the droplet is condensing onto the surfaces between and below the re-entrant structures and, when enough fluid has been deposited, forming a wetting pathway to the substrate, inducing a wetting transition. The latter mechanism is illustrated in Figure 16 and has been suggested by one study as feasible [32].

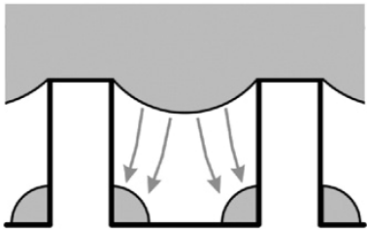

FIGURE 16: *The evaporating fluid from the underside of a Cassie droplet could potentially condense on the substrate and structures, eventually forming a wetting pathway and inducing a wetting transition to a Wenzel state. Image from [32].*

4 Experimental Methods and Materials

4.1 Setup Design

Imaging LOX droplets in non-boiling contact with LN_2-cooled surfaces requires that those surfaces be free of condensed liquids and, more importantly, ice, as these impurities can induce wetting transitions. The experiments presented in this work were carried out in a lab-built environmental chamber flushed with dry inert gas (nitrogen in this work, though any gas is possible).

This test environment mitigated both the problems of ice formation on the sample and droplet generator surfaces and also prevented the condensation of non-nitrogen atmospheric components (all have boiling points above nitrogen's) onto the sample surfaces. The existing environmental glove boxes in our lab are oxygen-free and thus were unsuitable for our experiments for obvious reasons. A simple glove box was therefore designed and fabricated in-house with the aid of the Nanotalo Machine Shop personnel. Nitrogen was chosen as the atmospheric gas due to its low cost, ease of availability, and sufficiently low boiling point (i.e., it will not condense onto surfaces cooled to 80–85 K). Only two other gases are feasible choices for the chamber atmosphere if cooler temperatures are desired in future works: neon (boiling point 27.07 K)[40] and helium (boiling point 4.22 K)[41].

Industry glove boxes of modest design still represent large costs for research labs (at least €1500 for suitable models, not including gloves), so a design based on the approach presented by [42] was utilized as a starting baseline. The total cost of our chamber is unknown as most of the materials were gathered from existing inventory, however. Special components (the sealed glove ports and oxygen shroud) were designed using FreeCAD and SolidWorks modeling software and subsequently 3D printed in ABS with an in-house MakerBot Replicator 2X 3D printer. Clear, 8 mm thick polycarbonate was used for the chamber walls for easy visual evaluation of experiments and to allow for external lighting and imaging. Simple vacuum plumbing components (Swagelok) were utilized for atmospheric inlet and outlets. The top panel was removable and a rubber strip created a seal with the chamber walls, providing ease of access to the experimental space for placing and/or removing larger objects. Simple tensioning straps were utilized to ensure the seal integrity even under positive internal pressure. The base and sidewalls were fastened and sealed at the edges with acrylic-based adhesive and wood screws. Figure 17 shows the chamber design and a photo of the experimental setup.

Typical droplet deposition techniques involve drawing a measured amount of room temperature fluid from a reservoir or syringe and depositing a droplet from a needle. However, this method is unworkable for cryoliquids unless the entire deposition system is kept in zero humidity at cryogenic temperatures, which would require a fully cooled cryostat. It was not possible to construct or purchase such a cryogenic chamber of the necessary size within the budget or time-frame of this project, so an alternative deposition method was devised. Liquid oxygen was chosen as the test fluid for several reasons: a) The liquid stable temperature range is wide enough (54–90 K) and can be easily reached with widely-available LN_2 cooling fluid, b) LOX is weakly paramagnetic and allows for magnetic manipulation of mobile droplets, and

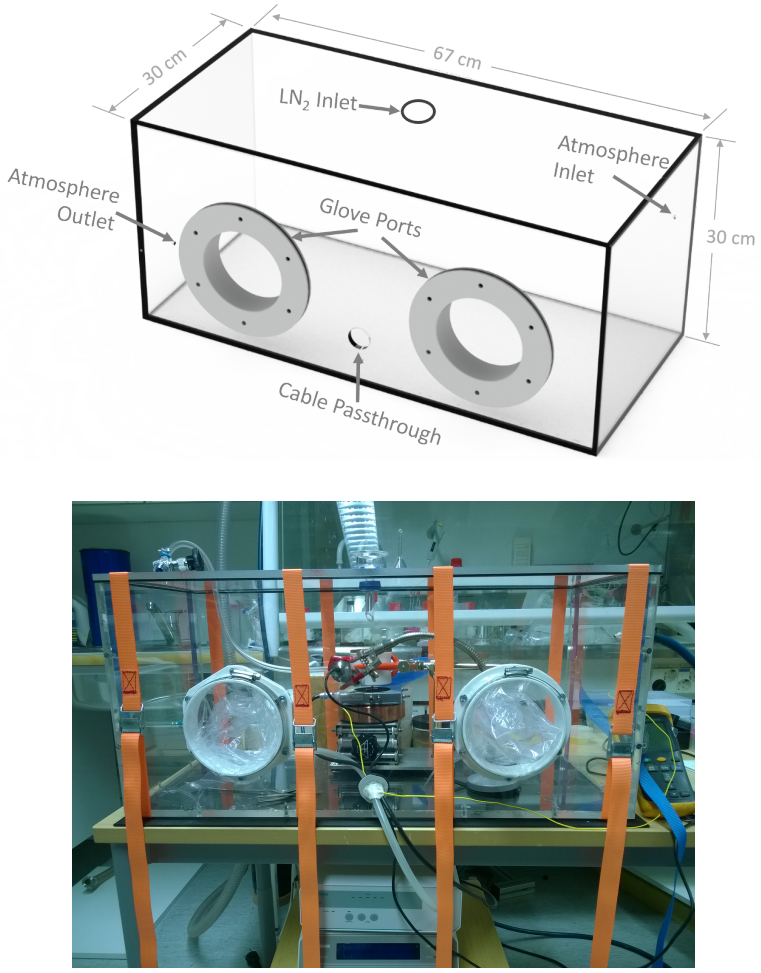

FIGURE 17: *Top image is the initial design, bottom is the fabricated chamber. Nitrogen dewar for substrate cooling not pictured. The chamber was designed in Solidworks and FreeCAD and fabricated from polycarbonate sheeting. The glove ports were designed in Solidworks and 3D printed from ABS. All mated surfaces at potential leak sites are sealed with Teflon tape, tack, or both. See the appendices for operating instructions and design details.*

c) it is relatively affordable and safe to handle in small quantities (see the supplemental information for safety precautions).

The LOX droplets were generated by controlled condensation onto a LN_2-cooled conic copper surface, based on the method described by Quéré [43], except the LOX was condensed from instrument-grade purity oxygen (instead of ambient air). A simple in-line valve was used manually to control the oxygen input flow rate. A typical droplet measured in this work had a radius

of 0.5–1.5 mm (about 2–5 µl). The condenser apparatus design can be seen in Figure 18 and consists of a machined copper cone with a 3–2 mm wall thickness (decreasing from flange to tip) resting within a cup-like shroud (3D printed from ABS). The oxygen displaces the gas in the shroud (nitrogen during experiments in the chamber) and condenses onto the cold copper surface. The wetting film of (now liquid) oxygen then travels through the ≈ 1.5 mm gap between the cone surface and the underside of the condenser cup and coalesces as a droplet at the sharp tip of the cone. The geometry of the tip self-regulates the droplet size under a constant pull force (defined by gravity plus any magnetic field present). It was noted that the distance of the condenser tip from a magnet drastically affected both the LOX droplet size and deposition rate given a constant supply of oxygen gas (or when operated in ambient air). An initial problem of excess oxygen gas flow resulting in condensed oxygen on the cold sample surfaces prior to droplet deposition was successfully mitigated by 3D printing and installing baffles inside and outside the shroud. Absorbent (and regeneratable) molecular sieve material (Zeolite) was also placed into the plastic shroud to absorb humidity introduced by the oxygen flow, resulting in a noticeable reduction of ice formation on the generator cone surface.

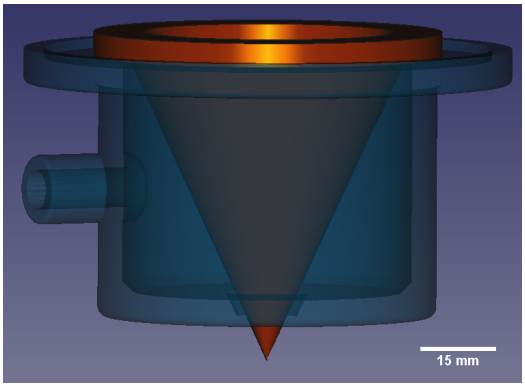

FIGURE 18: *The droplet condensation generator cone and shroud were designed in FreeCAD. The cone was machined from a copper billet and the shroud was 3D printed from ABS. The oxygen condenses onto the LN_2-cooled cone and coalesces at the tip as a droplet. 3D printed baffles (not shown) were later placed inside and outside the shroud to minimize oxygen condensation on substrates.*

4.2 Doubly Re-entrant Structures

The doubly re-entrant surfaces used in this work were fabricated on silicon wafers in the Micronova cleanroom. A deposited layer of SiO_2 was

first patterned to create the array geometry by standard wet photolithographic processing. An anisotropic inductively-coupled plasma reactive ion etch (ICP-RIE) step then created circular islands of silicon, the height of which ($\approx$ 1 µm) determined the cap height. SiO_2 was then again isotropically deposited by plasma enhanced chemical vapor deposition (PE-CVD) to form the 200–300 nm thin serif shapes of the doubly re-entrant caps. The arrays were patterned and etched again with another anisotropic RIE oxide etch step to isolate the caps from one another, followed by a deep ICP-RIE silicon etch to form the full height of the pillars. A final *isotropic* silicon etch step then reduced the pillar diameters until the stems were significantly thinner than the caps, completing the process. A more detailed overview of this process and the adjustments made to it during the course of this project can be found in the Supplemental Information (A). Additionally, one batch of 10 µm cap diameter samples were coated by CVD with a fluorinated silane self-assembled monolayer (SAM) coating with nanoscale thickness. The Cassie fractions of the samples were chosen to encompass a balance between the increased break-in pressure resistance of tightly packed structures and the higher contact angle repellency of lower Cassie fractions (predicted by the Cassie-Baxter model). The crucial dimensions of the serif cap structures were checked by ellipsometry measurements and by cross-sectional cutting of the pillar structures by focused ion beam milling (FIB), see Figure 19.

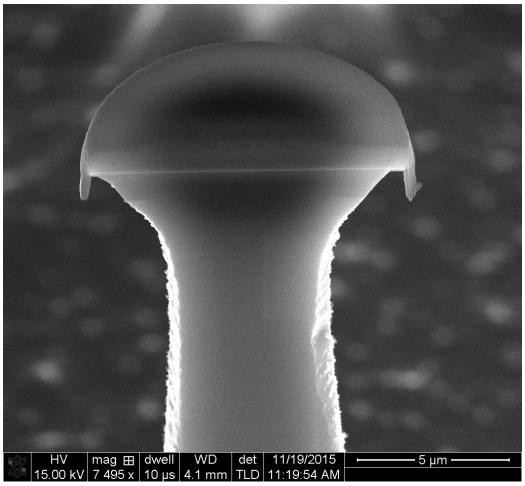

FIGURE 19: *A cross-section (cut by FIB) of an early 20 µm cap structure from an isometric view (the top of the structure is a flat semicircle).*

The fluoropolymer coating provided no apparent benefit in repelling LOX droplets, however it is feasible that this coating could reduce the rate of ice formation on the sample during cooling. Cap diameters of 10 and 20 µm with

array pitches of 20–60 µm and 80–120 µm, respectively, were fabricated and tested. It is noteworthy that the repellent cap structures are comprised of an intrinsically hydrophilic material, SiO_2, and the repellent properties of the surface stem entirely from the geometries of the arrays (pitch) and the structures (vertical overhangs) themselves. This is due to the pinning behavior of the three-phase contact line leading to more ideal surface tension force vectors resisting the wetting pressures (Laplace, gravitational, magnetic, etc.) on different geometries, as illustrated in Figure 20.

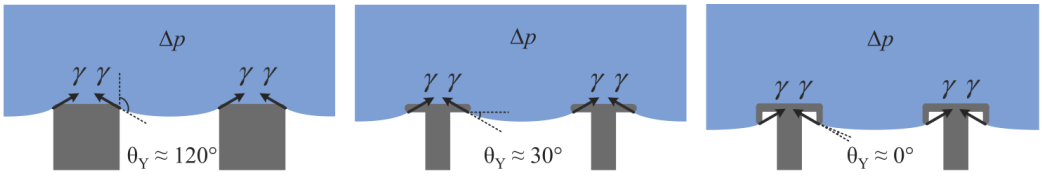

FIGURE 20: *Doubly re-entrant structures are an ideal shape for repelling fluids due to the vertical direction of the surface tension force vector at the pinning site compared to that of standard posts or singly re-entrant structures. Image from [3].*

The sample substrates (silicon wafer chips) were cooled using a microscopy cryo-stage (Linkam Scientific) thermal element removed from the stage casing. Liquid nitrogen flow from a small dewar placed in the chamber and a controllable resistive heater in the element provided accurate temperature monitoring and control. The actual surface temperature of the samples could not be measured, however silicone thermal grease was utilized to ensure good thermal contact with the element. The reason the surface temperature could not be determined directly is twofold: infrared camera thermometers typically do not provide accurate readings at cryogenic temperatures and the sample surfaces used here are too delicate for mechanical contact by a thermocouple lead. However, in theory, a well-calibrated, surface-mounted contact thermocouple could be utilized in future experiments as long as the sample surface is robust enough or is large enough to allow for direct contact with the sensor outside the structured area (current sample designs did not allow this). The total cooling capacity was confirmed, however, by cooling the element to 77 K and observing the condensation of stable liquid nitrogen on the sample surface from the atmosphere of the glove box, followed by its evaporation upon raising the set point temperature to 79 K. When depositing the liquid oxygen droplets, the surfaces were held at approximately an 80–85 K set-point both to avoid nitrogen condensation onto the surface and to quicken the evaporation of liquid oxygen upon a test failure (i.e., transition to a complete wetting state) in order to more quickly perform additional tests.

4.3 Measurement Procedure

Static measurements of contact angle (and confirmation of repellency) were attempted by depositing LOX droplets from the smallest height possible to reduce the impact pressure but with enough separation to allow for droplet "pinch-off" from the generator tip. CAH measurements were performed with droplets attached to the condenser tip, the advancing angle was measured by growing the droplet with a constant supply of oxygen until the contact radius expanded and the receding angle was measured similarly during droplet evaporation. Images and video were obtained from either a remotely controlled digital microscope (Dinolite AD7013MTL) inside the chamber or with a high speed camera (Phantom Miro 310) mounted outside the chamber. An adjustable, low heat, LED light diffusion panel was placed opposite the camera outside the chamber to provide consistent high contrast droplet back-lighting.

Due to the lack of successfully repelled free-standing liquid oxygen droplets, evaporation experiments were later carried out utilizing water droplets instead, using a Theta (Biolin Scientific) contact angle meter with a digitally controlled syringe pump to measure the contact angle and evaporation rates of freestanding droplets in ambient conditions. Five tests per sample pitch were performed with the 20 µm cap diameter samples. The droplet volumes and contact angles were recorded from the resulting image sequences using a custom Matlab script and the Attension software coupled to the contact angle meter, respectively. In order to best simulate the testing conditions used for liquid oxygen, the sample surfaces were heated to 80–90 $°C$. The surface temperature was monitored with an FLIR i5 infrared thermometer to ensure a constant and uniform substrate temperature during testing.

5 Results & Discussion

5.1 Non-Boiling Super-Repellency

Initial attempts at obtaining free-standing non-boiling liquid oxygen droplets were performed with 10 µm cap diameter samples, with pitches of 20, 30, 40, 50 and 60 µm, both with and without a fluoropolymer coating. Experiments were recorded both with a digital microscope (Dinolite AD7013MTL) at 5–20 frames/sec and with a high speed camera (Phantom Miro) at frame rates between 1000–10 000 frames/sec. Unfortunately, no sample from this set was able to support a Cassie state for a LOX droplet, even when the droplets were not free-standing (i.e., still attached to the droplet generator tip). All test failures consisted of an immediate and complete wetting of the substrate, no

Wenzel states were observed. Still frames of a LOX droplet wetting a sample surface from a high speed video can be seen in Figure 21. The transition to a completely wetted state ($\theta \approx 0°$) was instantaneous upon contact, determined to the limit of the high speed camera's framerate (10,000 frames/sec in this case). It can be seen in Figure 21 (and in the videos located in the supporting information) that the wetting LOX droplets do not boil upon contact with the sample, indicating the surfaces (including the oxide caps) are being cooled to a sufficiently low temperature ($< 90\,\mathrm{K}$).

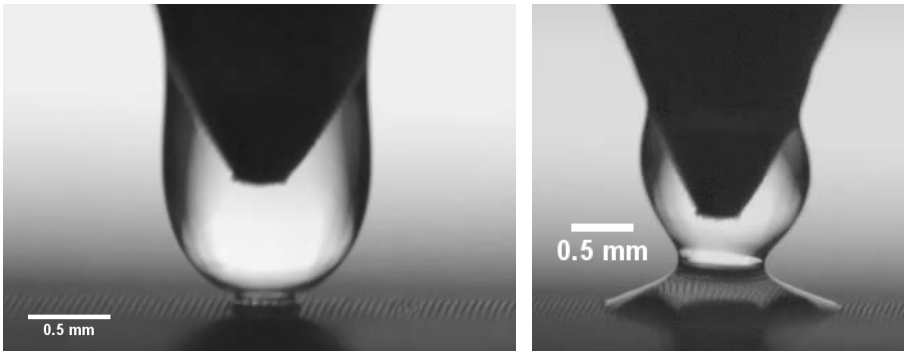

FIGURE 21: *Frames from a 10,000 fps high speed video showing a LOX droplet completely wetting a 10 µm cap diameter sample cooled to* $\approx 80\,\mathrm{K}$ *upon contact. Elapsed time between the frames is approximately 60 ms.*

Another set of samples containing re-entrant structures with approximately twice the height compared to all previous samples and caps of 20 µm diameter in arrays with pitches of 80, 100 and 120 µm was fabricated and tested with limited success. Two non-free-standing LOX droplets were successfully supported in a Cassie state on a small region of a 100 µm pitch sample, allowing for observations of both a droplet expanded until failure and a droplet allowed to evaporate until it was drawn off of the surface by surface tension back onto the generator cone. Videos recorded by the digital microscope allowed for an approximate manual determination of the advancing and receding contact angles and thus the CAH. Figure 22 shows a still-frame from each successful test along with the approximate contact angles (measured manually due to the irregular shape of the liquid column, that is, no algorithmic fit could be made). The apparent advancing (θ_{adv}) and receding (θ_{rec}) contact angles were measured to be 155–160° and 140–145°, respectively, the CAH is therefore approximately 10–20°, however this is only suggestive and more data from less error-prone measurement techniques are needed.

Additionally, the measured receding contact angle may be misleading and tests using a free-standing evaporating droplet are required, as the droplet

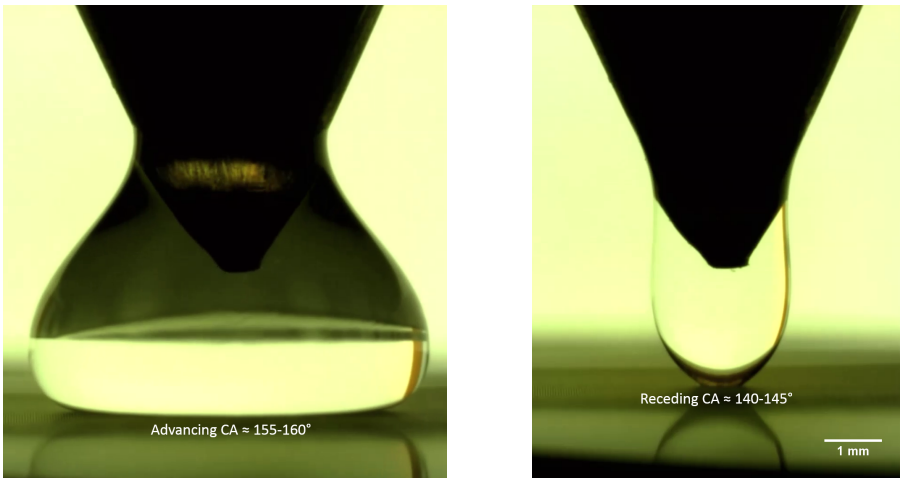

FIGURE 22: *Frames from digital microscope videos showing two successfully repelled (but not freestanding) LOX droplets on a 20 µm cap sample (100 µm pitch) both during expansion (left) and evaporation (right), allowing a manual approximation of the advancing/receding contact angles ($\theta_{\mathrm{adv}}/\theta_{\mathrm{rec}}$), respectively.*

generator tip may distort the droplet surface to such a degree as to exert force on the contact line during evaporation. The advancing contact angle should be more reliable as the pressure from the volume expansion would likely outweigh any forces resulting from the tip's deformation of the droplet's surface, however a recent study [6] has suggested that advancing contact angles are droplet size dependent and not reliable for characterizing structured repellent surfaces. It should be noted that the successful repulsion of non-free-standing LOX droplets was not able to be repeated (even with the same sample surfaces) during later testing for currently unknown reasons, which are speculated on in the next section.

It was determined by observing the sample surfaces under specific lighting conditions that certain regions of the samples were visually distinct from the rest of sample surface (see Figure 23). Further investigation by SEM revealed that the majority of the samples' array areas were missing the stem structures entirely due to an over-extensive final isotropic etch step, as described in the previous section. Manual testing with water and hexadecane droplets showed a clear distinction in wetting behavior between these areas. The areas with the missing structures were obviously unable to support even Cassie states for water droplets and were completely wetted by all tested fluids.

However, it should be noted that the intact regions of these samples *did* support stable Cassie states with water droplets, ethanol droplets ($\gamma = 21\,\mathrm{mN/m}$), and even FC-72 (when deposited gently) in ambient conditions.

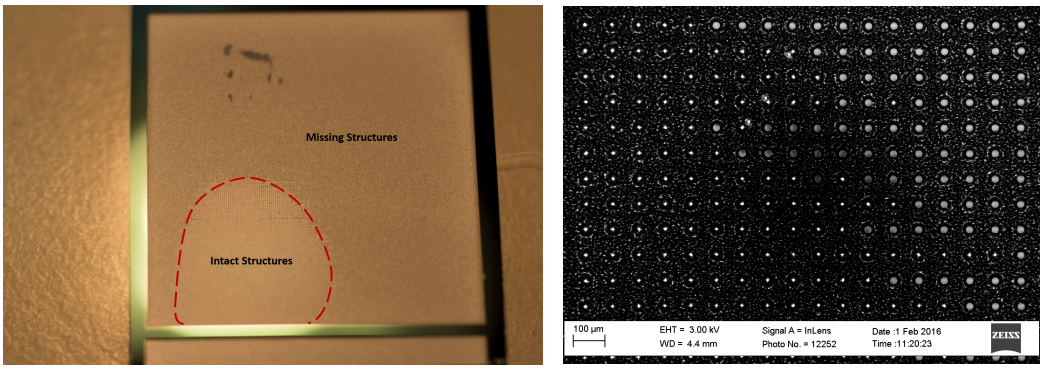

FIGURE 23: *The left image shows the visible difference between regions with and without intact structures, the right is an SEM image of the border between these regions where caps are visible more to the right.*

While no quantitative differences were seen in the limited contact angle data collected for such fluids between Cassie fractions, it was noted that manually depositing Cassie state droplets of low surface tension room-temperature fluids was more easily accomplished with the samples of medium Cassie fractions (100 µm pitch, 20 µm cap diameter).

5.1.1 Possible Causes of Cassie State Support Failure

The cause(s) for the failure of the 10 µm cap samples to support a liquid oxygen droplet in a Cassie state and the failure of the initial 20 µm samples to support a free-standing Cassie droplet are not apparent as of yet. There are, however, several hypotheses which could be confirmed or dismissed if a successful sample would eventually be fabricated. First, the initial sample pillars had comparatively short heights (≈ 25 µm) which could have caused a descending droplet to exert a pressure higher than the break-in pressure and contact the substrate in between pillars, thus initiating a wetting transition. While the break-in pressure limit described by equation 7 indicates the pillar heights were more than sufficient to support LOX droplets of the volumes utilized [3], it is possible that an impacting droplet of such a low surface tension fluid could generate enough pressure locally at the three-phase contact line on the pillars' top surfaces for the droplet to impale. Also, due to the irregular shapes and many defects seen in SEM images around the inner cap surfaces in the 10 µm cap structures, the droplet may not have needed to wet much further than the bottom of the re-entrant serif to encounter a defect and initiate a wetting transition.

Defect concentration may have also played a role in both the initial (10 µm) and later (20 µm) cap diameter samples, but the pillar height was

nearly doubled and the etching process times were adjusted in the later samples to ensure the structure arrays were free of the major defects seen in the initial samples (see Figure 24a). Figure 24c shows a representative doubly re-entrant cap from a later sample, only a slight "waviness" in the re-entrant serif can be seen. However, it seems unlikely, due to the smoothness and relatively small magnitude of the irregularity, that this slight defect alone would induce a wetting transition.

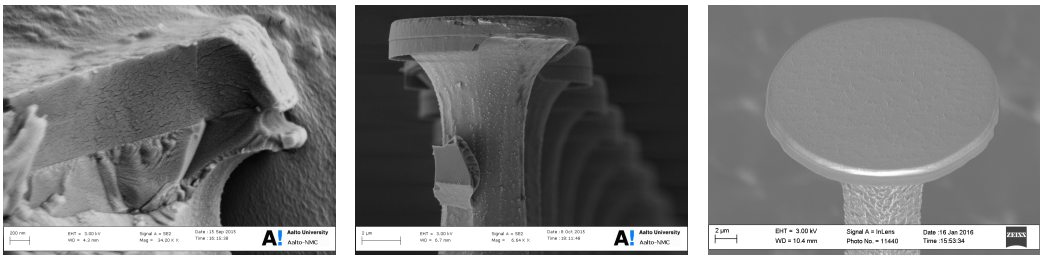

(A) *A sheared 10 µm cap.* (B) *An early 20 µm cap.* (C) *The latest 20 µm cap .*

FIGURE 24: *The presence of visible defects in earlier samples (a) was largely reduced in later samples. Initial defects were caused by non-optimal parameters during etching processes, while later defects' (damaged caps (b) and wavy serifs (c)) causes are unknown.*

Another hypothesis for the lack of Cassie state support suggests the liquid oxygen might be spreading along the oxide cap surface (due to the low contact angle ($\theta \approx 0°$) of LOX on SiO_2) and around the re-entrant structure, reaching the silicon post and traveling down to the substrate, creating a liquid path, the flow of which could induce a wetting transition. While this may seem unlikely due to the rapid evaporation rate of the LOX droplets, it cannot be discounted without further testing. A final hypothesis is simpler, suggesting merely that the environmental chamber is unable to reach a low enough humidity level and trace amounts of ice crystals are present on the surface, in effect dramatically increasing the defect concentration of the samples and leading to a higher likelihood of wetting transitions. It should be noted that, while the fluoropolymer coating appeared not to have a noticeable effect on the ability of the surfaces to repel LOX droplets, it is possible that the latter samples, which exhibited much fewer visible defects, could benefit from such a coating due to its potential ice-phobic properties.

The one-time success in repelling non-free-standing LOX droplets indicates the potential this experimental design holds for future research efforts. Further testing is required to confirm or discount any hypothesis regarding the observed wetting failure mechanism(s).

5.2 Water Droplet Evaporation

Water droplets were deposited onto and evaporated from the 20 µm cap samples' intact regions to confirm the expected pattern of increased evaporation time (i.e., slower heat transfer) with decreasing contact area. Water was utilized due to the lack of achievable free-standing LOX droplets using these samples. Figure 26 shows the evaporation curves and the linear result of scaling the volume data by equation 6, as suggested by Dash et al. [36] and Figure 25 shows the evolution of the contact angle during droplet evaporation. The latter figure displays the expected behavior of the contact angle decreasing until reaching the receding angle, at which point the contact radius begins to shrink and the well-known "stick-slip" behavior begins. Data shown in the plots was recorded only for first 90% of droplet volume loss in order to avoid the larger uncertainty inherent in analyzing very small droplets.

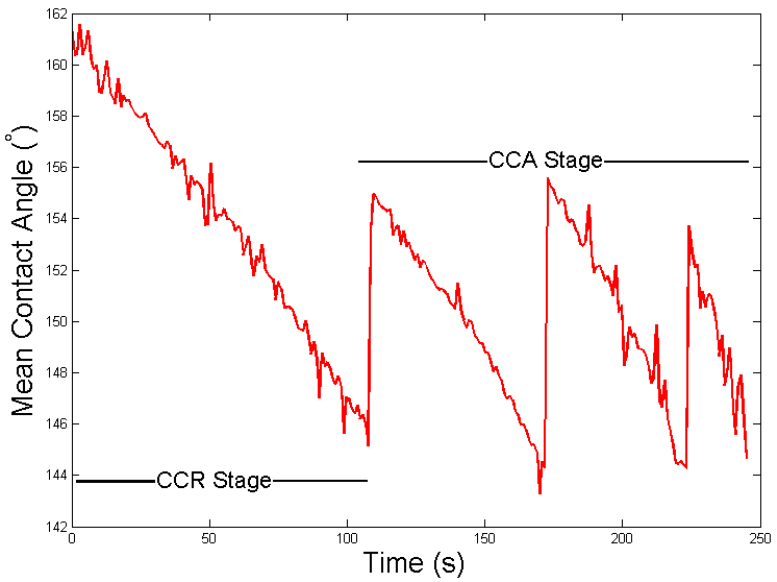

FIGURE 25: *The two stages of evaporation (CCR and CCA) are apparent for a representative water droplet on a 100 µm pitch sample, as is the vacillating CA indicative of stick-slip motion in the CCA stage.*

The Cassie fraction was determined by simply defining the area fraction of solid material on the sample as usual for any structured surface on which Cassie states are supported by the presence of air pockets, as described in section 2. However, with doubly-re-entrant samples, the total area in contact with the fluid also includes the outer vertical surface area of the re-entrant serif shape. This additional area, however, comprises just 6.3×10^{-3} µm^2 per 20 µm diameter cap, which is negligible compared to the area of the cap's

top surface, and thus can be safely ignored. Indeed, the serif's short height (see Figure 19 in the previous section) is designed to be $\approx 1\,\mu m$ in order to avoid significantly changing the surface's Cassie fraction. The effect of the overall surface Cassie fraction on the total evaporation time is illustrated in Figure 27. The height, thickness, and vertical angle of the serif structure are all crucial aspects of the doubly re-entrant design's repellent capacity.

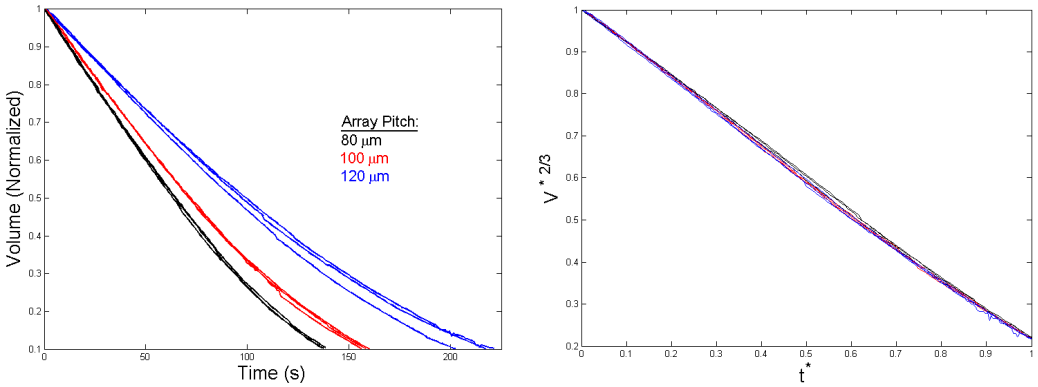

FIGURE 26: *The evaporation of water droplets was recorded, the relative volume change follows a 2/3 power law, which collapses the data in the right plot.*

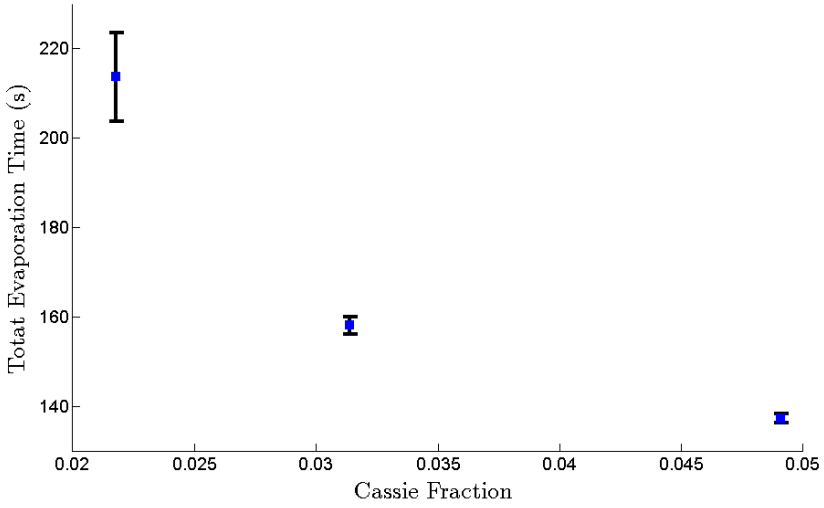

FIGURE 27: *Total evaporation time vs. sample Cassie fraction. Error bars are standard deviations from the mean for three tests on each sample.*

5.3 Conclusions

In this work droplets of liquid oxygen (LOX) have been deposited on cooled surfaces patterned with arrays of super-repellent doubly re-entrant nanostructures and imaged. The bulk of this work focused on designing and fabricating the experimental setup and developing the test methodologies, preliminary experiments were also performed and the results were presented. No free-standing, non-boiling LOX droplets were observed, however two non-free-standing droplets were observed and analyzed, showing a contact angle of $\approx 140°$ and a CAH of $\approx 20°$ for one doubly re-entrant sample. While these values indicated repellent behavior, they did not indicate *super*-repellent behavior ($\theta > 150°$, CAH $< 5°$). Hypotheses on the causes for the observed failure were presented and mitigation possibilities were suggested.

The limited success seen with the samples fabricated so far suggests further testing should be performed as the sample fabrication procedures continue to be refined. If samples are fabricated which can reliably support Cassie states with LOX droplets, then repeatable measurements of static, advancing, and receding contact angles should taken, as well as the determination of sliding angle with a rotating sample jig. Testing of the evaporation time of droplets should be conducted in the same manner as for the water droplets. To this end, a wide range of Cassie fractions (both by varying cap diameter and structure pitch) should be fabricated to further probe the effects of surface geometry on evaporative heat transfer. If free-standing droplets evaporate too quickly for meaningful analysis, reducing the sample surface temperature to 77–78 K is possible, however, in order to avoid nitrogen condensation, neon or helium should be utilized for atmospheric flushing instead. If samples could be fabricated supporting low enough CAH such that the LOX droplets were highly mobile, then sliding friction oscillation experiments should be performed as described in the next section, as this would provide more representative data for comparison with ferrofluid oscillation data. Finally, the break-in pressure should be determined using either falling droplets with varying Weber numbers (by altering the release height) or equilibrium droplets in an increasingly strong magnetic field (either by bringing a permanent magnet closer to the substrate or by utilizing a variable electromagnet).

6 Oscillating Leidenfrost Droplets

6.1 Background

A droplet in a *Leidenfrost state* can be observed when the surface is heated to the Leidenfrost temperature for that particular fluid-surface pair, at which point the droplet will reach the film boiling state and hover on a cushion of its own evaporating vapor flux, as illustrated in Figure 28. The Leidenfrost temperature is unique to each surface-fluid combination and is difficult to predict exactly [44]. The Leidenfrost point for water on a metal surface is approximately $240\,°C$, but for cryoliquids, Leidenfrost droplets can be observed on room temperature surfaces.

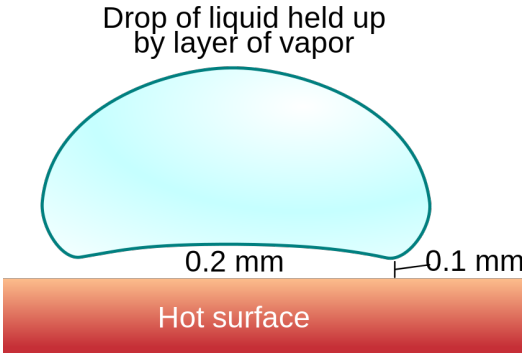

FIGURE 28: *A droplet in a Leidenfrost state hovers over the substrate on a cushion of its own evaporative vapor flux. The geometry of the vapor gap is determined by the droplet size and is thinnest at the rim of the droplet's underside. Image from Wikipedia.*

In the Leidenfrost state, the heat transfer rate from the substrate to the droplet decreases dramatically, as the conduction pathway is cut off and the supporting vapor layer acts as thermal insulation. Therefore, a Leidenfrost droplet will evaporate at a slower rate than a droplet in a Cassie state on a heated repellent surface. It has also been shown [45] that Leidenfrost droplets floating above various surfaces can evaporate at significantly varied rates, a super-repellent structured surface with a low Cassie fraction will transfer less heat to the droplet than a flat repellent surface and the Leidenfrost droplet lifetime can again be increased significantly.

The size of a Leidenfrost droplet has an important influence on the geometry of its supporting vapor layer. Very small droplets can be approximated as spheres, but for larger droplets, the vapor layer has a non-uniform thickness,

being thinner around the outer rim of the droplets underside and thicker towards the center. For very large droplets (with a radius much larger than the capillary length), this non-uniformity increases in magnitude and eventually the evaporated gas at the center of the droplet's underside cannot escape to the edges and bubbles up through the center of the droplet, forming what is called a "chimney" [44]. This causes turbulent flow within the droplets which can yield interesting flow dynamics and coherent surface oscillations, resulting in droplets shaped into non-circular geometries as viewed from above. While this phenomenon is interesting and has been studied in detail, the rapid and semi-chaotic movements can also inhibit clear imaging of long-lived Leidenfrost droplets, as small droplets, which avoid this behavior, are relatively short-lived. In this work, imaged Leidenfrost droplets of LOX were unable to be measured accurately (or precisely) enough to record meaningfully comparable evaporation curves. The droplet edges were blurred by the rapid oscillations induced by the instabilities in the supporting vapor layer.

A unique property of Leidenfrost droplets is the extremely low friction inhibiting their lateral motion on a flat surface. This allows for interesting studies of nearly ideal Newtonian dynamics in one or two dimensions, hydrodynamics of droplet motion on room temperature liquid surfaces [46], and in the case of LOX, studies of the interaction of magnetic forces and fluid dynamics (see Figure 29). The paramagnetism of liquid oxygen droplets in Leidenfrost states was utilized by Quéré et al. to study the dynamics of droplet deformation in a magnetic field and even droplet motion as an orbital mechanics analogue due to the magnetic attractive force scaling with the same inverse square of distance which governs gravitational attraction for celestial bodies [43, 44].

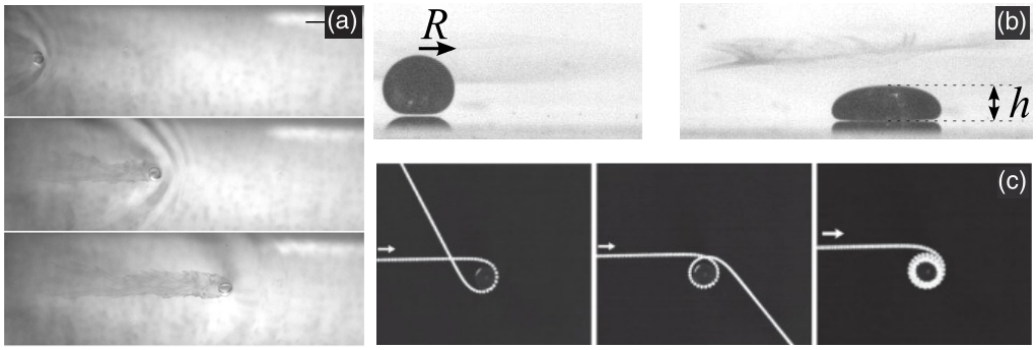

FIGURE 29: *LOX droplets in Leidenfrost states have been used to investigate wave drag dynamics on liquid surfaces (a, droplet is LN_2), droplet deformation in varying magnetic field strengths (b), and even orbital mechanics (c, light paths are droplet trajectories). Image A from [47], B from [43], C from [46].*

The vapor layer under a Leidenfrost droplet has been shown to be resistant to breakdown from external forces, the droplet may flatten and spread, but the average vapor layer thickness does not significantly decrease even under highly increased gravity [48] or strong magnetic fields [43]. There is a small effect on the Leidenfrost temperature for a given fluid-surface pair under large external forces due to the thinning of the vapor layer at the thinnest point around the "rim" of the droplet's underside [48]. Additionally, the evaporation time is reduced as the droplet spreads under the influence of external forces due to the increased "contact" area supported by the vapor layer leading to increased heat transfer to the droplet.

6.2 Experimental Methods

The paramagnetism exhibited by liquid oxygen droplets has been utilized by Quéré et al., in whose work LOX droplets in Leidenfrost states were captured and dynamically manipulated with simple magnet configurations. Such studies allow for studying analogues of planetary dynamics as the magnetic force on the droplet scales with the inverse square of the distance from the magnet, similar to the gravitational force on celestial bodies. In this work, preliminary experiments were performed in which droplets were imaged while oscillating along a single dimension in a parabolic magnetic field, exhibiting lightly damped simple harmonic motion. The experimental technique utilized was developed originally for the work of Timonen and Latikka [12], in which superparamagnetic ferrofluid droplets oscillated on superhydrophobic surfaces in the presence of a rare-earth (N52 grade) magnet.

The flushing of the environmental chamber with nitrogen in this work allowed for experiments using instrument-grade (99.999% pure) oxygen (rather than the impure LOX condensed from air in the work of Quéré), minimized the formation of ice on the surfaces, and prevented the formation of condensed clouds of water vapor around the measurement area, which hamper clear imaging of Leidenfrost droplets. Using pure oxygen also allows for a more uniform magnetization from droplet to droplet, minimizes the risk of solid impurities inducing contact with the substrate, and ensures a uniform surface tension to better compare experimental results. The thermal element utilized for cooling the super-repellent surfaces described earlier was also used as a heating element to keep the supporting surfaces at room temperature. Vacuum grease was applied between the thermal element and the samples to ensure good thermal contact. A high speed camera operating at 1000 frames per second was utilized to capture videos of the oscillating droplets. The captured image sequences were analyzed with custom Matlab scripts which utilize image processing techniques to locate the droplet, record the centroid

position and volume data, and finally, fit a simple harmonic model to the data with given properties of the droplet fluid.

The model equation fit to the data is an analytic solution to the harmonic oscillator equation

$$m\ddot{x} = -kx - F_\eta \pm F_\mu,$$

taking into account viscous ($F_\eta = 2\beta\dot{x}$) and sliding friction (F_μ) damping forces for a free, damped oscillator. See the supplemental information in [12] for a detailed derivation of this model. From the model fit several parameters of interest could be extracted, namely the oscillation period, viscous and friction dissipation coefficients (β and μ, respectively), and the spring constant (k) of the system:

$$k = \mu_o V c \left[M + H\left(dM/dH\right)\right],$$

where μ_o is permeability of free space, V is droplet volume, H is spatially dependent magnetic field strength, M is droplet magnetization, and c is the field curvature (steepness of the magnet's potential well). The damping friction force (F_μ) was also calculated from the results. Finally, the recorded and smoothed position data was used to extract velocity, kinetic and potential energy, and power dissipation data.

Initial experiments were performed according to the procedure described by Timonen and Latikka, with the droplet deposited at the edge of the magnetic potential onto a glass slide (see Figure 30). However, unlike the ferrofluid droplet experiments, the LOX droplets failed to travel along a uniform path (initially aligned with the focal plane of the camera) or even in a straight line at all, but rather either traced shallow ellipses and/or straight but rotating paths. The cause of this behavior is due to the confluence of extremely low friction, slight non-uniformities in the parabolic magnetic field, and unavoidable slight tilting of the substrates. The magnitude of these deviations was small enough that portions of a few measured oscillations could be successfully analyzed, however there was no possibility of comparison between measurements or repeatability to improve certainty in the calculation of oscillation parameters.

To improve oscillation repeatability, a small aluminum v-track was designed (see the supplemental information (A)) to act as a one-dimensional guide for the droplets. Previous attempts at using v-tracks made from 3D printed ABS and machined PTFE (Teflon) failed to support Leidenfrost states due to local surface cooling. This component will not facilitate the characterization of flat surfaces as the ferrofluid experiments [12] do, but it will enable studies on the effects of substrate temperature, geometry, and the

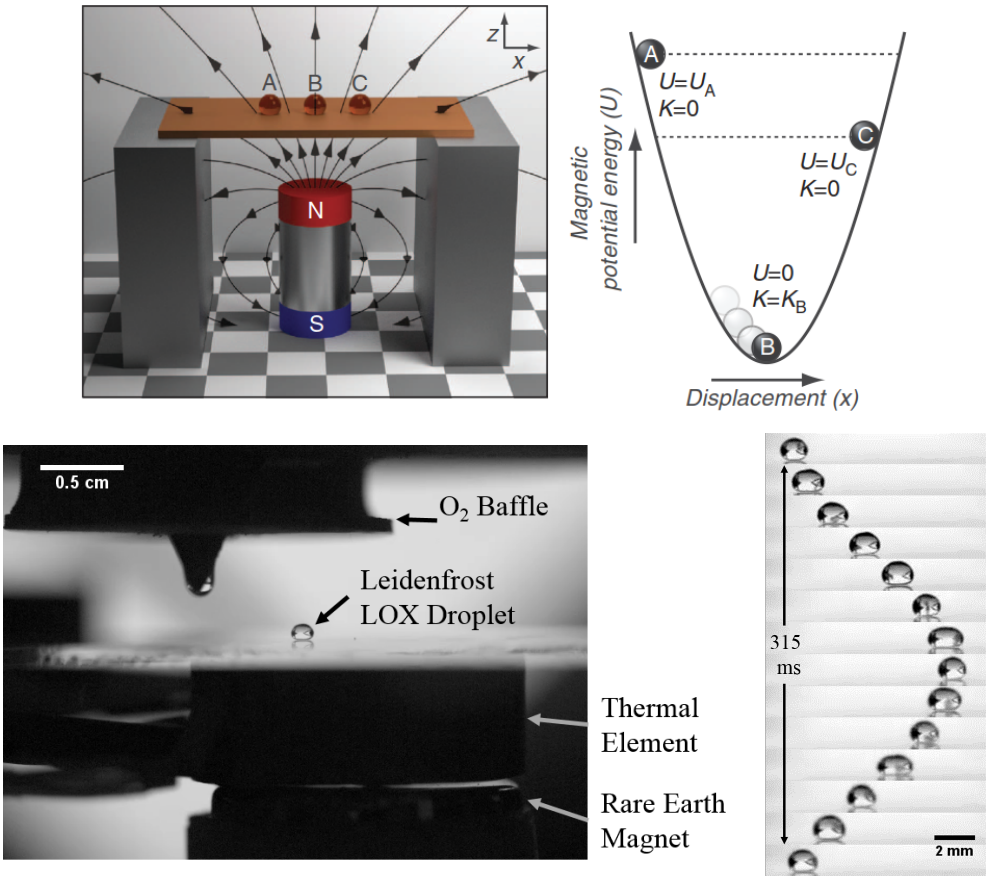

FIGURE 30: *Our experimental method for droplet oscillation analysis was initially developed for ferrofluid droplets (top). A droplet is deposited at the edge of a parabolic magnetic potential and allowed to oscillate freely on a room temperature surface. Top image from [12].*

force gradient magnitude/configuration for droplets of any fluid in Leidenfrost states. *(This component has not been fabricated at the time of writing due to time constraints during this thesis.)* If utilized, the aluminum guide should be heated for approximately 30 minutes prior to measurements and kept at 20–30 $^{\circ}C$ during the experiment to avoid ice formation in the bottom of the v-track.

6.3 Results & Discussion

The oscillation position data was recorded and a subset of harmonic oscillations (those with amplitudes between tunable limits) were extracted for analysis. The simple harmonic model used in this work was initially devel-

oped for aqueous ferrofluid droplets and failed to fit the LOX droplet data at first, as it did not take into account the far more rapid evaporation rate of LOX compared to aqueous ferrofluid. To that end, the code was modified to fit the model to overlapping or sequential slices of the measured droplet position data, within each of which the change in droplet volume was assumed to be negligible. Thus, for each slice, an average droplet mass was calculated and assumed to be unchanging. The determination of the "width" of these slices was based on a trade-off, as narrower slices better approximate constant volume within themselves and thus better correct for the effects of evaporation, while achieving a good fit to the data requires a minimum number of full oscillations included in the slice. Two full oscillations were included in each "slice" in the calculation results presented here. The overlapping version of the fitting process begins each slice at a turning point (local maxima/minima where the droplet is changing direction) and thus provides more data points and a more continuous picture of the evolution of the oscillation parameters; the separated version simply divides the data into disparate slices, allowing for direct comparisons between segments of the data and providing a continuous set of unique smoothed data points over the range of the entire measurement, which is then useful for later calculations of velocity, energy, and power dissipation. Figure 31 illustrates the differences between these methods and shows the improvement in the fitting quality compared to the initial single fitting approach. As parameters are calculated in the model for each fit, the new approaches also allowed visualization of the evolution of the oscillation parameters as the droplet evaporated. It should be noted that the evaporation for Leidenfrost LOX droplets was linear, as opposed to the nonlinear behavior seen for Cassie-state droplets in the previous section. This behavior stems from the insulating vapor layer, which reduces the heat transfer rate from the substrate and therefore reduces the magnitude of the temperature (and thus evaporative flux) gradient throughout the droplet.

Additionally, velocity data was pulled from the position data and used to generate energy and power dissipation plots, which could again be compared to ferrofluid droplet oscillation data. The data show approximately an order of magnitude reduction (10^{-8} to 10^{-9} J/W) in total energy and power dissipation when compared to ferrofluid droplet oscillation data on superhydrophobic surfaces, as was expected. Figure 32 shows the energy and power dissipation curves for the oscillating droplet.

The viscous and friction forces extracted from the harmonic oscillator model fit have slightly different meanings than those for the ferrofluid droplets the model was developed for. Namely, the sliding friction force for ferrofluid can be referred to as the contact angle hysteresis force, however, for Leidenfrost droplets there is no contact line, thus this force is representative of

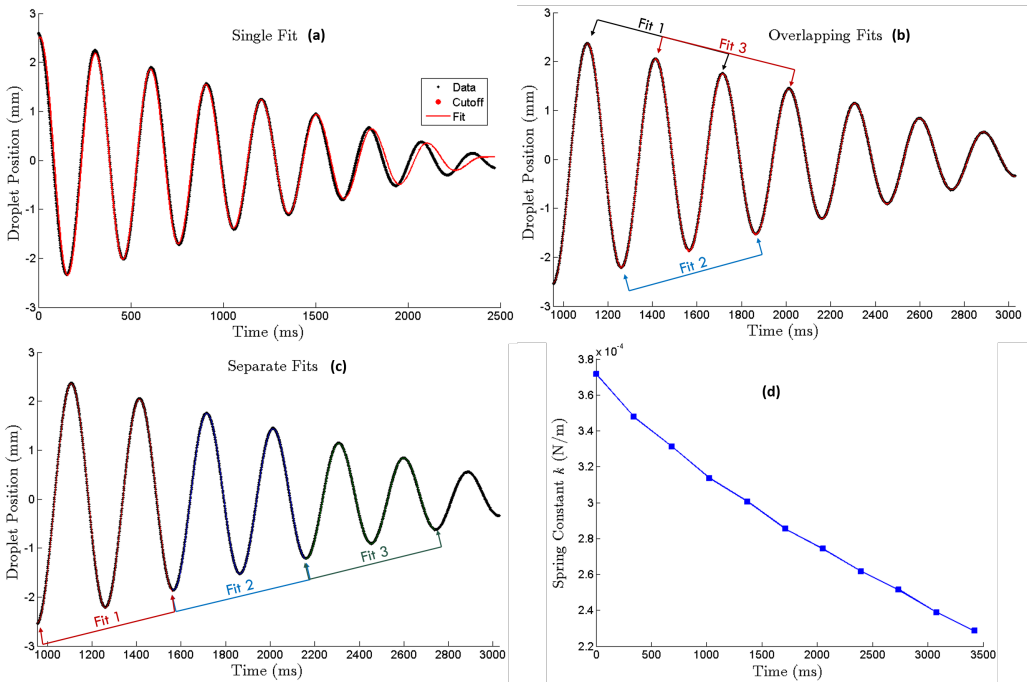

FIGURE 31: *The oscillation position data is fitted with a harmonic oscillator solution (see [12]). Fitting all data simultaneously (a) failed due to significant droplet evaporation. Splitting the data into overlapping (b) or separate (c) slices provided a better fit and allowed for the visualization of oscillation parameter evolution. The observed decreasing spring constant (k) value (d) is consistent with theory, assuming a constant dm/dt. The slight deviation from linearity near the start is due to increased uncertainty in volume determination caused by large droplet deformations.*

the drag forces on the underside surface of the droplet resulting from gas turbulence in the thin supporting vapor layer. This "friction" force and the inertial viscous drag force, scale with $\eta V h^{-1} R^2$ and $\rho V^2 R l_c$ [43, 44], respectively, where η is viscosity, V is velocity, h is the vapor film thickness, and R is the droplet radius. The friction force is typically smaller by an order of magnitude compared to the viscous drag force until the velocity becomes very small. The friction forces calculated from the experimental data for LOX droplets in this work match the scale of this prediction (10–100 nN), thus indicating the potential viability of using the harmonic oscillator model for Leidenfrost droplets, although further testing with repeatable data is needed to fully validate the model.

Further experiments could investigate the effects of varying magnetic field strength, surface structure and/or temperature, and, if doubly re-entrant

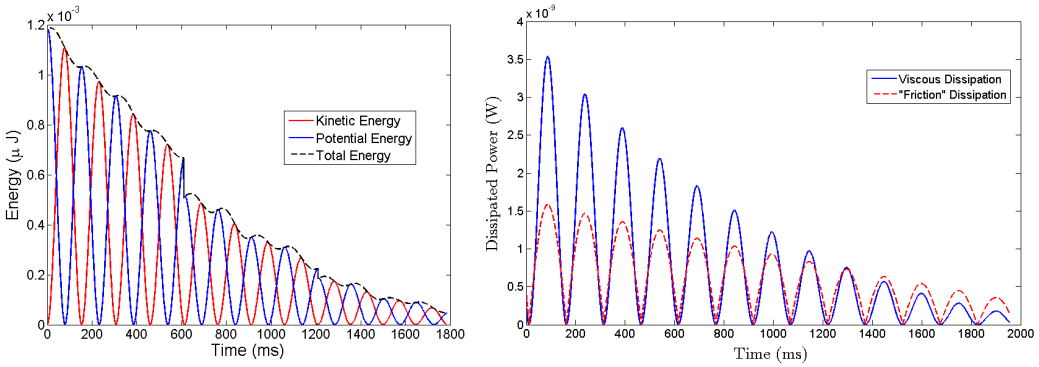

FIGURE 32: *The smoothed position data from the separated slice fitting allows for calculations kinetic/potential energies and power dissipation. The magnitude of the energy and power dissipation is approximately one order lower than that of ferrofluid droplets on superhydrophobic surfaces, consistent with theoretical predictions. The two discontinuities in the energy plot are due to slight inaccuracies in the model fit endpoints for the data slices.*

samples are fabricated capable of supporting Cassie state droplets with low CAH, oscillation experiments with cooled substrates (not Leidenfrost droplets) could produce results more directly comparable to ferrofluid droplet data.

It has been suggested [45] that structured super-repellent surfaces may allow Leidenfrost droplets to transition to non-boiling Cassie states upon cooling of the substrate due to reduced heat transfer (avoiding boiling); if a room temperature surface supporting a Leidenfrost LOX droplet could be cooled quickly enough (to $< 90\,\mathrm{K}$) while avoiding ice formation, it might be possible to facilitate an extremely gentle deposition of the droplet, leading to potentially successful support of a Cassie state LOX droplet. This approach could avoid wetting failure mechanisms triggered by impact pressure dynamics.

6.4 Conclusions

Oscillation experiments utilizing paramagnetic LOX droplets were performed by a modified methodology originally developed for ferrofluid droplets on superhydrophobic surfaces, showing promise for future low friction droplet oscillation experiments. Future Leidenfrost experiments can improve upon the developed methods and experimental setup in order to achieve test repeatability. Oscillations on warm liquid surfaces (inspired by [47]) can also be explored, as can the effects of magnetic field strength and/or surface parameters on evaporation rates of Leidenfrost droplets.

References

[1] Christian Dorrer and Jurgen Ruhe. Some thoughts on superhydrophobic wetting. *Soft Matter*, 5:51–61, 2009. doi: 10.1039/B811945G. URL http://dx.doi.org/10.1039/B811945G.

[2] A. Susarrey-Arce, A. G. Marin, H. Nair, L. Lefferts, J. G. E. Gardeniers, D. Lohse, and A. van Houselt. Absence of an evaporation-driven wetting transition on omniphobic surfaces. *Soft Matter*, 8:9765–9770, 2012. doi: 10.1039/C2SM25746G. URL http://dx.doi.org/10.1039/C2SM25746G.

[3] Tingyi "Leo" Liu and Chang-Jin "CJ" Kim. Turning a surface superrepellent even to completely wetting liquids. *Science*, 346(6213): 1096–1100, 2014. ISSN 0036-8075. doi: 10.1126/science.1254787. URL http://science.sciencemag.org/content/346/6213/1096.

[4] Zhiwei Wang and Tianzhun Wu. Modeling pressure stability and contact-angle hysteresis of superlyophobic surfaces based on local contact line. *The Journal of Physical Chemistry C*, 119(23):12916–12922, 2015. doi: 10.1021/jp512930d. URL http://dx.doi.org/10.1021/jp512930d.

[5] Tingyi Leo Liu, Zhiyu Chen, and Chang-Jin Kim. A dynamic cassie-baxter model. *Soft Matter*, 11:1589–1596, 2015. doi: 10.1039/C4SM02651A. URL http://dx.doi.org/10.1039/C4SM02651A.

[6] Frank Schellenberger, Noemí Encinas, Doris Vollmer, and Hans-Jürgen Butt. How water advances on superhydrophobic surfaces. *Phys. Rev. Lett.*, 116:096101, Feb 2016. doi: 10.1103/PhysRevLett.116.096101. URL http://link.aps.org/doi/10.1103/PhysRevLett.116.096101.

[7] Juuso T. Korhonen, Tommi Huhtamäki, Olli Ikkala, and Robin H. A. Ras. Reliable measurement of the receding contact angle. *Langmuir*, 29 (12):3858–3863, 2013. doi: 10.1021/la400009m. URL http://dx.doi.org/10.1021/la400009m.

[8] Graham Walker. *Cryocoolers: Part 2: Applications*. Springer Science & Business Media, 2012.

[9] R. Nave. Heat blocking by vacuum flask walls. URL http://hyperphysics.phy-astr.gsu.edu/hbase/thermo/vacfla.html#c3. HyperPhysics Online Resource.

[10] Joseph J. Jasper. The surface tension of pure liquid compounds. *Journal of Physical and Chemical Reference Data*, 1(4):841–1010, 1972. doi: http://dx.doi.org/10.1063/1.3253106. URL `http://scitation.aip.org/content/aip/journal/jpcrd/1/4/10.1063/1.3253106`.

[11] E. C. C. Baly and F. G. Donnan. Xciii.-the variation with temperature of the surface energies and densities of liquid oxygen, nitrogen, argon, and carbon monoxide. *J. Chem. Soc., Trans.*, 81:907–923, 1902. doi: 10.1039/CT9028100907. URL `http://dx.doi.org/10.1039/CT9028100907`.

[12] Jaakko VI Timonen, Mika Latikka, Olli Ikkala, and Robin HA Ras. Free-decay and resonant methods for investigating the fundamental limit of superhydrophobicity. *Nature Communications*, 4, 2013.

[13] H. Yildirim Erbil. The debate on the dependence of apparent contact angles on drop contact area or three-phase contact line: A review. *Surface Science Reports*, 69(4):325 – 365, 2014. ISSN 0167-5729. doi: http://dx.doi.org/10.1016/j.surfrep.2014.09.001. URL `http://www.sciencedirect.com/science/article/pii/S0167572914000223`.

[14] A.J.B. Milne and A. Amirfazli. The cassie equation: How it is meant to be used. *Advances in Colloid and Interface Science*, 170(1–2):48 – 55, 2012. ISSN 0001-8686. doi: http://dx.doi.org/10.1016/j.cis.2011.12.001. URL `http://www.sciencedirect.com/science/article/pii/S0001868611001928`.

[15] S. Moulinet and D. Bartolo. Life and death of a fakir droplet: Impalement transitions on superhydrophobic surfaces. *European Physical Journal E – Soft Matter*, 24(3):251 – 260, 2007. ISSN 12928941. URL `http://search.ebscohost.com/login.aspx?direct=true&db=afh&AN=27956212&site=ehost-live`.

[16] Edward Bormashenko. Progress in understanding wetting transitions on rough surfaces. *Advances in Colloid and Interface Science*, 222:92 – 103, 2015. ISSN 0001-8686. doi: http://dx.doi.org/10.1016/j.cis.2014.02.009. URL `http://www.sciencedirect.com/science/article/pii/S0001868614000530`. Reinhard Miller, Honorary Issue.

[17] Xuemei Chen, Justin A Weibel, and Suresh V Garimella. Water and ethanol droplet wetting transition during evaporation on omniphobic surfaces. *Scientific Reports*, 5, 2015.

[18] Lichao Gao and Thomas J. McCarthy*. How Wenzel and Cassie were wrong. *Langmuir*, 23(7):3762–3765, 2007. doi: 10.1021/la062634a. URL `http://dx.doi.org/10.1021/la062634a`.

[19] G. McHale*. Cassie and Wenzel, Were they really so wrong? *Langmuir*, 23(15):8200–8205, 2007. doi: 10.1021/la7011167. URL `http://dx.doi.org/10.1021/la7011167`.

[20] Abraham Marmur and Eyal Bittoun. When Wenzel and Cassie are right: Reconciling local and global considerations. *Langmuir*, 25(3): 1277–1281, 2009. doi: 10.1021/la802667b. URL `http://dx.doi.org/10.1021/la802667b`.

[21] C. W. Extrand and Sung In Moon. Contact angles of liquid drops on super hydrophobic surfaces: Understanding the role of flattening of drops by gravity. *Langmuir*, 26(22):17090–17099, 2010. doi: 10.1021/la102566c. URL `http://dx.doi.org/10.1021/la102566c`.

[22] C. W. Extrand and Sung In Moon. When sessile drops are no longer small: Transitions from spherical to fully flattened. *Langmuir*, 26(14): 11815–11822, 2010. doi: 10.1021/la1005133. URL `http://dx.doi.org/10.1021/la1005133`.

[23] R.L. Cerro. Contact angles: Laplace-young equation and dupre-young relationship. El Instituto de Matemática Aplicada del Litoral (IMAL).

[24] *Laplace-Young and Bashforth-Adams Equations*. First Ten Angstroms, November 2000. Application Note.

[25] Francis Bashforth and John Couch Adams. *An attempt to test the theories of capillary action: by comparing the theoretical and measured forms of drops of fluid*. University Press, 1883.

[26] Z. N. Xu. An algorithm for selecting the most accurate protocol for contact angle measurement by drop shape analysis. *Review of Scientific Instruments*, 85(12), 2014. doi: http://dx.doi.org/10.1063/1.4903198. URL `http://scitation.aip.org/content/aip/journal/rsi/85/12/10.1063/1.4903198`.

[27] Andrew J Milling. *Surface characterization methods: principles, techniques, and applications*, volume 87. CRC Press, 1999.

[28] A.F. Stalder, G. Kulik, D. Sage, L. Barbieri, and P. Hoffmann. A snake-based approach to accurate determination of both contact

points and contact angles. *Colloids and Surfaces A: Physicochemical and Engineering Aspects*, 286(1–3):92 – 103, 2006. ISSN 0927-7757. doi: http://dx.doi.org/10.1016/j.colsurfa.2006.03.008. URL http://www.sciencedirect.com/science/article/pii/S0927775706002214.

[29] Siddarth Srinivasan, Gareth H. McKinley, and Robert E. Cohen. Assessing the accuracy of contact angle measurements for sessile drops on liquid-repellent surfaces. *Langmuir*, 27(22):13582–13589, 2011. doi: 10.1021/la2031208. URL http://dx.doi.org/10.1021/la2031208.

[30] Maurizio Santini, Manfredo Guilizzoni, and Stephanie Fest-Santini. X-ray computed microtomography for drop shape analysis and contact angle measurement. *Journal of Colloid and Interface Science*, 409:204 – 210, 2013. ISSN 0021-9797. doi: http://dx.doi.org/10.1016/j.jcis.2013.06.036. URL http://www.sciencedirect.com/science/article/pii/S0021979713005894.

[31] Yuehua Yuan and T Randall Lee. Contact angle and wetting properties. In *Surface Science Techniques*, pages 3–34. Springer, 2013.

[32] Hans-Jürgen Butt, Ilia V. Roisman, Martin Brinkmann, Periklis Papadopoulos, Doris Vollmer, and Ciro Semprebon. Characterization of super liquid-repellent surfaces. *Current Opinion in Colloid & Interface Science*, 19(4):343 – 354, 2014. ISSN 1359-0294. doi: http://dx.doi.org/10.1016/j.cocis.2014.04.009. URL http://www.sciencedirect.com/science/article/pii/S1359029414000478.

[33] Yi-Lin Hung, Yao-Yuan Chang, Meng-Jiy Wang, and Shi-Yow Lin. A simple method for measuring the superhydrophobic contact angle with high accuracy. *Review of Scientific Instruments*, 81(6), 2010. doi: http://dx.doi.org/10.1063/1.3449325. URL http://scitation.aip.org/content/aip/journal/rsi/81/6/10.1063/1.3449325.

[34] H. Yildirim Erbil. Evaporation of pure liquid sessile and spherical suspended drops: A review. *Advances in Colloid and Interface Science*, 170(1–2):67 – 86, 2012. ISSN 0001-8686. doi: http://dx.doi.org/10.1016/j.cis.2011.12.006. URL http://www.sciencedirect.com/science/article/pii/S0001868612000036.

[35] N.M. Kovalchuk, A. Trybala, and V.M. Starov. Evaporation of sessile droplets. *Current Opinion in Colloid & Interface Science*, 19(4):336 – 342, 2014. ISSN 1359-0294. doi: http://dx.doi.org/10.1016/j.cocis.

2014.07.005. URL http://www.sciencedirect.com/science/article/pii/S135902941400082X.

[36] Susmita Dash and Suresh V. Garimella. Droplet evaporation dynamics on a superhydrophobic surface with negligible hysteresis. *Langmuir*, 29 (34):10785–10795, 2013. doi: 10.1021/la402784c. URL http://dx.doi.org/10.1021/la402784c.

[37] Susmita Dash and Suresh V. Garimella. Droplet evaporation on heated hydrophobic and superhydrophobic surfaces. *Phys. Rev. E*, 89:042402, Apr 2014. doi: 10.1103/PhysRevE.89.042402. URL http://link.aps.org/doi/10.1103/PhysRevE.89.042402.

[38] Thomas M Schutzius, Stefan Jung, Tanmoy Maitra, Gustav Graeber, Moritz Köhme, and Dimos Poulikakos. Spontaneous droplet trampolining on rigid superhydrophobic surfaces. *Nature*, 527(7576):82–85, 2015.

[39] Wei Xu, Rajesh Leeladhar, Yong Tae Kang, and Chang-Hwan Choi. Evaporation kinetics of sessile water droplets on micropillared superhydrophobic surfaces. *Langmuir*, 29(20):6032–6041, 2013. doi: 10.1021/la400452e. URL http://dx.doi.org/10.1021/la400452e.

[40] E Ao Guggenheim. The principle of corresponding states. *The Journal of Chemical Physics*, 13(7):253–261, 1945.

[41] C. Vicente, W. Yao, H. J. Maris, and G. M. Seidel. Surface tension of liquid he^4 as measured using the vibration modes of a levitated drop. *Phys. Rev. B*, 66:214504, Dec 2002. doi: 10.1103/PhysRevB.66.214504. URL http://link.aps.org/doi/10.1103/PhysRevB.66.214504.

[42] The construction of the ucsc econo-box: An inexpensive yet effective glove box. *Journal of Chemical Education*, 78(11):1513, 2001. doi: 10.1021/ed078p1513. URL http://dx.doi.org/10.1021/ed078p1513.

[43] Keyvan Piroird, Baptiste Darbois Texier, Christophe Clanet, and David Quéré. Reshaping and capturing leidenfrost drops with a magnet. *Physics of Fluids*, 25(3):032108, 2013. doi: http://dx.doi.org/10.1063/1.4796133. URL http://scitation.aip.org/content/aip/journal/pof2/25/3/10.1063/1.4796133.

[44] D. Quéré. Leidenfrost Dynamics. *Annual Review of Fluid Mechanics*, 45:197–215, January 2013. doi: 10.1146/annurev-fluid-011212-140709.

[45] Ivan U Vakarelski, Neelesh A Patankar, Jeremy O Marston, Derek YC Chan, and Sigurdur T Thoroddsen. Stabilization of leidenfrost vapour layer by textured superhydrophobic surfaces. *Nature*, 489(7415):274–277, 2012.

[46] Marie Le Merrer, Christophe Clanet, David Quéré, Élie Raphaël, and Frédéric Chevy. Wave drag on floating bodies. *Proceedings of the National Academy of Sciences*, 108(37):15064–15068, 2011. doi: 10.1073/pnas.1106662108.

[47] Keyvan Piroird, Christophe Clanet, and David Quéré. Magnetic control of leidenfrost drops. *Phys. Rev. E*, 85:056311, May 2012. doi: 10.1103/PhysRevE.85.056311. URL `http://link.aps.org/doi/10.1103/PhysRevE.85.056311`.

[48] L. Maquet, M. Brandenbourger, B. Sobac, A.-L. Biance, P. Colinet, and S. Dorbolo. Leidenfrost drops: Effect of gravity. *EPL (Europhysics Letters)*, 110(2):24001, 2015. URL `http://stacks.iop.org/0295-5075/110/i=2/a=24001`.

A Supplemental Information

A.1 Experimental Procedures

This section is to serve as a baseline guide for future researchers utilizing the experimental setup described in this work for similar exercises. Step-by-step instructions will be given for both the repellency testing and Leidenfrost measurements along with added suggestions for improvements or additions to increase the versatility of the setup for non-related research. ***Be sure to read the safety precautions at the end of this section before attempting unsupervised experimentation!***

A.1.1 Setup

- The environmental chamber should sit on a flat, vibration-free surface with two layers of rubber sheeting underneath. The straps used for maintaining the seal on the top panel should be laid between these layers to minimize slippage (some movement will still occur though, these sheets could be replaced by better non-slip surfaces).

- The 6 mm holes located on the side panels are sized to accept a Swagelok 6 mm tube connector tightly wrapped in 2 to 3 layers of Teflon thread-locking tape. Connect the inlet and outlet fittings for the atmospheric gas(es) to these inlets. An oil bubbler was used as a one-way outlet in this work, however a vacuum pump (pulling light vacuum only) can also be connected if desired (note: the chamber will not support a high vacuum). The pressure in the chamber could be measured, but would require a much more sensitive detector, in this work slight positive pressures were detected by observing the gloves as they inverted and inflated.

- The gloves should be free of holes and tight when stretched over the port flanges; hold them in place with hose clamps. The fingertips should reach the back of the chamber but not much beyond, as this will make putting one's hands into them difficult.

A.1.2 Before Sealing the Top Panel

- Make sure to place and clean (with isopropanol or ethanol to remove adsorbed moisture) all needed items within the box before tightening the straps. This includes samples, nitrogen dewars, handling tools, magnets, absorbent materials, humidity/temperature sensors, etc.

- Orient the sample stage, thermal element, magnets, droplet generator and cameras as well, as these tasks are made difficult by the constraints of the gloves.
- This done, tighten all six straps, two around the long dimension and four around the short dimension. Ensure tightness and check the seal around the perimeter of the top panel for any misalignments or gaps.
- Then the inlet atmospheric gas valve may be turned on to the desired flowrate and allowed to flush for the necessary time. In our setup, the nitrogen 2.5 line connected to a 6 mm Swagelok valve turned 0.5 turns could reach sub-2% humidity after a minimum of one hour. This time is affected by atmospheric humidity in the laboratory, of course.
- *Improvement Idea*: Cracking around the screws in the walls discouraged the use of draw hasps around the top panel, but if this can be avoided or the chamber is rebuilt with tougher materials, such hardware would simplify and improve the sealing procedure. See the design reference [42] for an example.

A.1.3 Generating LOX Droplets

- *Cold Surfaces Only*: Loading/Changing Samples: When using a thermal element to cool a sample surface down to LN_2 temperatures, first wait until the humidity is at a minimum, then heat your surface to the highest safe temperature it can handle (don't go over $250\,°C$ if you have a nitrogen dewar connected) for a minimum of 10 minutes (more is better) to drive off any adsorbed moisture, keep the nitrogen flush going during this time. This will minimize ice formation on your samples, especially important for samples with intricate micro/nanostructures. Allow the heated element to cool to approximately room temperature by shutting off the resistive heating. This slow cooling will avoid thermal shock. Upon reaching room temperature, you can begin the cooling process, using the Linkam flow controller and/or the heating control to reach and maintain a specific temperature (assuming you are using the TMS91 model, the newer model (TMS94) allows for easier control but did not work with our particular stage). This must be done in between each sample. One can also heat all the samples at the beginning of the experiment, however, if vacuum grease is utilized, removal of a sample from an element at cryogenic temperatures could be impossible, as would forming a good contact with the stiff, frozen grease with a new sample. This heating step could also be done

for Leidenfrost measurements if localized ice formation from adsorbed moisture under the floating cryoliquid droplets is a concern.

- Once the humidity has reached the desired level, the thermal element may be activated using the Linkam temperature controllers (LN_2 flow for cold samples, the appropriate heat for Leidenfrost measurements) and the generator cone can be cooled. If deemed necessary, place any absorbent material (e.g., Zeolite) within the shroud to minimize ice formation on the condenser surface. Zeolite is a molecular sieve which needs to be heated at $\approx 200\,^{\circ}\mathrm{C}$ in vacuum for several hours to regenerate its absorbent properties after prolonged use.

- Cooling the generator cone is accomplished by carefully pouring LN_2 through the funnel installed in the top panel. Tubing may be used for flow redirection if the generator cannot be placed directly under the funnel. Utilize an additional, smaller funnel inside the more permanently installed larger one (with a gap maintained by any support structure (tack was used in this work)) to allow for the backflow of nitrogen gas during pouring, otherwise the flow rate will be limited and LN_2 will spill chaotically outside the chamber. During this pouring process, the atmospheric gas flow should be kept low but not off, to prevent the liquid nitrogen pushing in atmospheric humidity. Plug the larger funnel with tack when not pouring as well. It will take approximately 5 to 15 minutes to fully cool the copper generator, depending on the rate of LN_2 addition. A violent boil-over will signify that sufficiently low temperatures have been reached (this is, obviously, when the Leidenfrost layer in the cone has collapsed). Refill the generator as needed throughout the experiments.

- At this point, the condensing gas (oxygen in our work) is allowed to flow in using the valves setup. First, the valve near the source is opened to "prime the line" (do this once or twice before the condenser is cooled to flush any residual humidity), the pressure gage will indicate the presence of the gas in the line. Then the second valve can be turned to allow small amounts of the gas at a time. This setup avoids interrupting the flow to other instruments. Producing a single drop manually is somewhat difficult, but can be achieved with practice.

- *Improvement Idea*: Manual flow control is difficult to use for single droplet generation. Installing a low pressure, programmable mass flow controller in place of the inlet valve would drastically improve not only

the ease of use, but also allow for precise and repeatable droplet size control.

A.1.4 Shutting Down

- When measurements are complete, if possible, do not unseal the chamber.
- Flush the oxygen line and close its valves, allow the thermal element to cool/warm to room temperature, run the atmospheric gas for a short time to flush any remaining traces of oxygen, and leave open any containers of remaining liquid nitrogen inside the chamber (the pressure of the evaporation will escape through the outlet).

A.1.5 Analyzing Leidenfrost Droplet Oscillations

- Droplet oscillations should be filmed from the side using a high speed camera ideally operating at 1000 frames/second at the highest possible resolution. Zoom in as closely as possible on the droplet and use a light panel for back-lighting.
- It is crucial to ensure the flatness of the substrate if the v-track droplet guide is not being utilized in order to ensure the droplet oscillates only within the focal plane of the camera.
- Once the video is obtained, it can be analyzed for droplet position and size using a small library of Matlab scripts. Contact angle data must be obtained separately from individual frames using any image analysis tool (ImageJ plugin (e.g., DropSnake), Attension software, etc.).
- The videos can either be converted to a thresholded binary using the *videothreshold.m* function to determine the correct threshold value, otherwise the conversion can be done prior to analysis manually (this is often faster and more convenient) using VirtualDub (or any other video editing software).
- The preferred function running order is first *dropcentroid.m*, then *OscillatorMiro.m*, and finally *oscillationperiod.m*. If the fluid being tested is volatile (evaporates significantly during the oscillations), it is best to then run the *stepfit.m* function, as the model fit provided by the previous function assumes a constant droplet volume and will result in a poor fit to the final sections of the data.
- Consult the functions' header instructions for more details.

A.2 Potential Improvement Ideas

There are several potential areas of improvement that can and should be worked on for the experimental setup.

- The top panel is currently sealed with a rubber stripping and hand-tightened straps that maintain the seal in the presence of slight positive pressures. The original design calls for the use of draw hasps (see [42]), but the polycarbonate used for the walls exhibited cracking from the screws installed in the corners, so utilizing the hasps was not a possibility. These would allow for a tighter seal and much more convenient access into the chamber, but would require the chamber to be rebuilt (highly suggested, regardless) with tougher polycarbonate (or other clear polymer). The rubber stripping should also be replaced as it will develop cracks over time and should be arranged such that the corners overlap (they currently do not).

- In this work, 2.5 grade nitrogen was used to flush the chamber and reduce humidity to avoid ice formation on cooled sample surfaces. However, it was often seen that trace amounts of ice still formed, though not consistently and without obvious cause, even when the humidity was measured to be at the lower limit of the meter ($\approx$2%). Several potential improvements could be made: 1) Use a more sensitive humidity sensor to characterize drying performance, 2) Install fans to circulate the gases inside the chamber to avoid pockets of humid air being left behind in the corners, 3) Utilize an in-line drying system (e.g., Zander Ecodry) on the atmospheric nitrogen inlet if it is determined that the trace amounts of water vapor in the nitrogen are the cause of the icing issue (this is doubtful, but possible), 4) Utilize a "cold finger", a LN_2-cooled metal object inside the chamber as both a "cryo-pump" of sorts and/or as a qualitative humidity sensor.

- The current cable pass-through is a simple hole plugged by a conic rubber pass-through, the gaps around the cables and the plug itself are just plugged with tack. This is obviously an inelegant and non-versatile solution. A proper cable pass-through can be designed in to the next iteration of the chamber, such components are readily available from any laboratory or industrial vacuum supplier and require only a specifically sized hole for installation.

- A v-track component has been designed that should allow a droplet to oscillate within a single plane in a 3D magnetic parabolic potential.

It should be heated to remove any adsorbed moisture before use and maintained at room temperature with the thermal element. The component should be machined from aluminum, plastic parts were shown not to support Leidenfrost states.

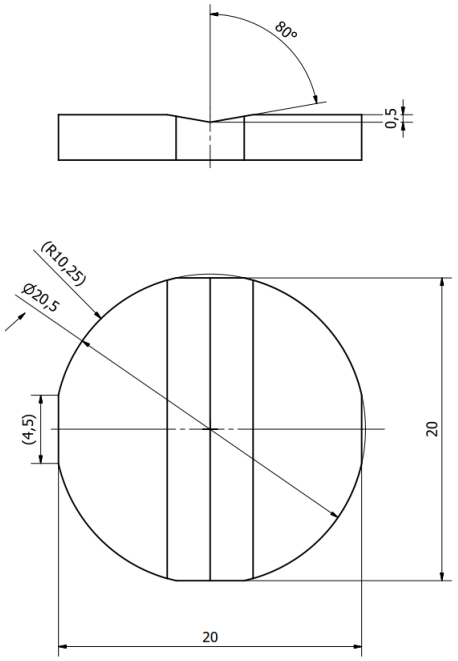

FIGURE 33: *V-track design, dimensions in mm.*

A.3 Doubly Re-entrant Structure Fabrication Process

This is a more detailed overview of the fabrication process (and the changes made to it) than is found in the main text, but individual process parameters (times, temperatures, pressures, exact chemistries, etc.) are not included here. Consult the Microfabrication group in Micronova (headed by Dr. Sami Franssila), specifically Ville Rontu as he carried out the fabrication in the cleanroom, for specific processing details.

Wafers are standard silicon wafers (i.e., not SOI). *PE-CVD*: Plasma Enhanced Chemical Vapor Deposition; *ICP-(D)RIE*: Inductively Coupled Plasma (Deep) Reactive Ion Etching; *PE-ALD*: Plasma Enhanced Atomic Layer Deposition.

1. PE-CVD SiO_2 deposition to 1 µm thickness.

2. Spin coating of positive photoresist.

3. Patterning of photoresist by UV light exposure through mask and removal of unpatterned resist by washing.

4. Etching of exposed oxide by anisotropic RIE and removal of remaining (patterned) resist. Creates circular oxide islands.

5. Anisotropic ICP-RIE of exposed silicon to 1 µm depth. Creates circular silicon islands topped with oxide. Traditional gas chemistry is SF_6 + O_2, later samples utilized addition of CHF_3 to improve control of vertical etching angle.

6. Isotropic PE-CVD deposition of oxide to 200–300 nm thickness. Forms the vertical "serif" shape of the caps. Initial samples utilized PE-ALD instead of PE-CVD.

7. Spin coating and UV patterning of positive photoresist, followed by an anisotropic RIE step and finally removal of photoresist. Removes the oxide layer between the cap structures, isolating the caps.

8. Anisotropic ICP-DRIE of exposed silicon to pillar height depth. Pillar diameter is uniform from cap to substrate at this point.

9. *Isotropic* ICP-RIE of silicon to thin the silicon stems in relation to the oxide caps, forming the final doubly re-entrant structures. The time and gas flow parameters in this step resulted in the non-uniform, defective regions of later samples.

10. *For fluorinated silane SAM coating*: Oxygen plasma treatment to clean and coat the surface with hydroxyl groups, followed by heated immersion in a small amount of $1H$,$1H$,$2H$,$2H$-perfluorodecyltrichlorosilane in a closed petri dish at $80\,°C$ for 3 hours.

Deposition thicknesses were confirmed with ellipsometry measurements and overall pillar dimensions were confirmed by SEM image analysis, direct profilometer measurements, and cross-sectional FIB milling. Samples utilized in this work were obtained by careful manual crystallographic plane splitting of the wafers to obtain samples small enough to allow for thermal control (samples larger in area than the cooling element proved impossible to cool sufficiently, resulting in immediate nucleate boiling of LOX droplets on contact).

A.4 Safety Precautions & Warnings

A.4.1 Gases

While working, make sure the area is fully ventilated and be conscious of any possible gas leaks. If you begin to feel tired, weak, light-headed, or get a slight headache, immediately open a vent/window/etc., shut off any gases, and leave the area until the feeling subsides, as this is an early indication of oxygen deprivation. Likely leak sites are the gloves/glove ports, top-panel seal, gas inlet/outlet fittings and possibly the gas lines themselves.

When finished with any experiment, position an open vent nearby in case of a leak as nitrogen displacement of air in a small room is a life-threatening hazard, and an oxygen leak (however unlikely using this setup) poses additional flammability and explosion risks if left open for long periods of time. While an explosion would require very concentrated oxygen levels, keep in mind that the barrier to combustion for any flammable material (and some normally non-flammable ones too!) begins to decrease at a volume concentration of 23% oxygen (normal oxygen (in air) concentration is $\approx 21\%$).

Fully check that there is no possibility of gas leakage (especially oxygen) by checking each valve, hose, and connection before leaving the area!

A.4.2 Cryoliquids

Handling cryoliquids also poses a safety risk, both from air displacement resulting from evaporative expansion (1:694 (liquid:gas) for LN_2, 1:861 for LOX) and from contact tissue freezing.

Always wear gloves when handling pitchers or dewars and use thermal insulated gloves when directly handling cooled items (this should not ever be necessary). Wear eye protection when pouring liquid nitrogen as backsplash is common. The Leidenfrost effect offers some protection from small amounts of cryoliquids in fleeting contact (e.g., spray, small droplets), but mucous membranes such as eyes can still be damaged by larger amounts and/or prolonged contact.

Always ventilate the area directly adjacent to any open containers of liquid nitrogen.

Leftover liquid nitrogen should be left to evaporate under a vent or in a fume hood, or safely disposed of outdoors.